Spring 2015

Modeling and analysis of a resonant nanosystem

Scott L. Calvert
Purdue University

Graduate School Form 30
Updated 1/15/2015

PURDUE UNIVERSITY
GRADUATE SCHOOL
Thesis/Dissertation Acceptance

This is to certify that the thesis/dissertation prepared

By Scott L. Calvert

Entitled
Modeling and Analysis of a Resonant Nanosystem

For the degree of Master of Science in Mechanical Engineering

Is approved by the final examining committee:

Dr. Jeffrey F. Rhoads
Chair

Dr. Saeed Mohammadi

Dr. Charles M. Krousgrill

To the best of my knowledge and as understood by the student in the Thesis/Dissertation Agreement, Publication Delay, and Certification Disclaimer (Graduate School Form 32), this thesis/dissertation adheres to the provisions of Purdue University's "Policy of Integrity in Research" and the use of copyright material.

Approved by Major Professor(s): Dr. Jeffrey F. Rhoads

Approved by: Dr. Ganesh Subbarayan 4/22/2015
Head of the Departmental Graduate Program Date

MODELING AND ANALYSIS OF A RESONANT NANOSYSTEM

A Thesis

Submitted to the Faculty

of

Purdue University

by

Scott L. Calvert

In Partial Fulfillment of the

Requirements for the Degree

of

Master of Science in Mechanical Engineering

May 2015

Purdue University

West Lafayette, Indiana

ACKNOWLEDGMENTS

Thank you to my advisor, Dr. Jeff Rhoads, for constantly being available for questions, as well as for his patience and guidance throughout the process of developing this work, despite the often faced setbacks and mistakes.

Thank you to Dr. Andrew Sabater, for his step-by-step guidance and continuous, thought-provoking questions as I slowly began to learn what was involved with properly thinking about NEMS.

Thank you to Yanfei Shen and Hossein Pajouhi, for their patience throughout the experimental process, and their assistance in understanding and using the simulator.

This thesis is based in part upon work supported by the National Science Foundation under grant numbers 1233780 and 1247893. Any opinions, findings, and conclusions or recommendations expressed in this document are those of the author and do not necessarily reflect the views of the National Science Foundation.

TABLE OF CONTENTS

LIST OF TABLES

Table Page

LIST OF FIGURES

ABSTRACT

Calvert, Scott L. MSME, Purdue University, May 2015. Modeling and Analysis of a Resonant Nanosystem. Major Professor: Jeffrey F. Rhoads, School of Mechanical Engineering.

The majority of investigations into nanoelectromechanical resonators focus on a single area of the resonator's function. This focus varies from the development of a model for a beam's vibration, to the modeling of electrostatic forces, to a qualitative explanation of experimentally-obtained currents. Despite these efforts, there remains a gap between these works, and the level of sophistication needed to truly design nanoresonant systems for efficient commercial use. Towards this end, a comprehensive system model for both a nanobeam resonator and its related experimental setup is proposed. Furthermore, a simulation arrangement is suggested as a method for facilitating the study of the system-level behavior of these devices in a variety of cases that could not be easily obtained experimentally or analytically.

The dynamics driving the nanoresonator's motion, as well as the electrical interactions influencing the forcing and output of the system, are modeled, experimentally validated, and studied. The model seeks to develop both a simple circuit representation of the nanoresonator, and to create a mathematical system that can be used to predict and interpret the observed behavior. Due to the assumptions used to simplify the model to a point of reasonable comprehension, the model is most accurate for small beam deflections near the first eigenmode of the beam.

The process and results of an experimental investigation are documented, and compared with a circuit simulation modeling the full test system. The comparison qualitatively proves the functionality of the model, while a numerical analysis serves to validate the functionality and setup of the circuit simulation. The use of the simulation enables a much broader investigation of both the electrical behavior and the

physical device's dynamics. It is used to complement an assessment of the tuning behavior of the system's linear natural frequency by demonstrating the tuning behavior of the full nonlinear response. The simulation is used to demonstrate the difficulties with the contemporary mixing approach to experimental data collection and to complete a variety of case studies investigating the use of the nanoresonator systems in practical applications, such as signal filtering. Many of these case studies would be difficult to complete analytically, but results are quickly achieved through the use of the simulation.

CHAPTER 1. INTRODUCTION

1.1 Background

The advantages that resonant micro/nanoelectromechanical systems (M/NEMS) provide in comparison to their purely-electrical counterparts, such as higher quality factors and narrower resonant bandwidths [1], has led to their proposed use in a variety of applications ranging from tunable filters [2], logic elements [3], self-oscillators [4] and transistors [5, 6] to microscopic radios [7, 8] and mass sensors [9–12]. Working towards these ends, researchers have made a variety of advancements in M/NEMS to streamline their fabrication [13–17], model their performance, and, to a limited extent, enable design [1, 4–9, 11, 13, 14, 16, 18–24, 24–48].

As the basic understanding of different device designs has developed, the need to begin looking at how to implement devices in their proposed end-use scenarios has grown. Such efforts began on a single-device scale for many systems [8, 34], but there is a pressing need to begin building the infrastructure for the design and fabrication of these devices at a mass production rate and in a very large scale integration (VLSI) context, in a fashion similar to existing electrical components. In order to achieve this, there is a need for accurate, system-level electromechanical models of M/NEMS. This need points to experimentally-verified, first-principles based models as opposed to phenomenological descriptions, because of the need to account for device behavior under a wide variety of input and operating conditions.

In order to achieve mass production, and VLSI use, of M/NEMS, the model of any device must be able to accurately integrate with other electrical components to predict a system-level response. Stopping at developing a model to represent the velocity or displacement of M/NEMS will likely fail to provide insight into even the qualitative nature of the electrical response, as shown in [40]. Likewise, a model that only describes the currents driven by the dominant electromechanical transduction mechanism can fall short of describing the true response by ignoring the feedback and damping of the full circuitry involved. Therefore, experimentation and modeling efforts must account for the full electrical system of the test setup to allow for the later extraction of an isolated device model that could be correctly implemented with any other circuitry. The use of the various model components and system-level effects in a standard commercial circuit simulator, along with the use of a hardware description language such as Verilog-A, allows for faster verification and tuning of the model behavior when comparing to experimental results [49, 50]. It also serves as a direct pathway to the later use of the device model on a larger scale. This method provides an open door for the evaluation of the next steps towards practical implementations of a device, such as impedance matching or filter design, because of the ease with which the device model can be integrated into a larger system model.

1.2 Project Goals

This work further develops the understanding of the nanoresonator systems originally presented in [14], and described in the following section. A first-principles based model to describe the beam's mechanical and electrical dynamics is developed. Experimental data is used to qualitatively verify the performance of the model and thereby justify the understanding of how the electromechanical system operates. This model is studied to determine the practical benefits and use cases that separate this nanoresonator design from those presented in the prior work. Nonlinear system behavior can be obtained even at low forcing voltages [47], which allows for intriguing behaviors such as the electrostatic tuning of the resonant frequency [48] with slight changes in the input. Features such as this pose an interesting design challenge while also being a powerful tool for circuit developers. As the model is developed, the analysis seeks to focus on the system-level response, not merely the beam dynamics. Studying the variations in the system output and their correlation to differing inputs and system configurations will lead to several proposed uses and cautionary statements related to the practical application of these nanoresonator systems.

1.3 System Description

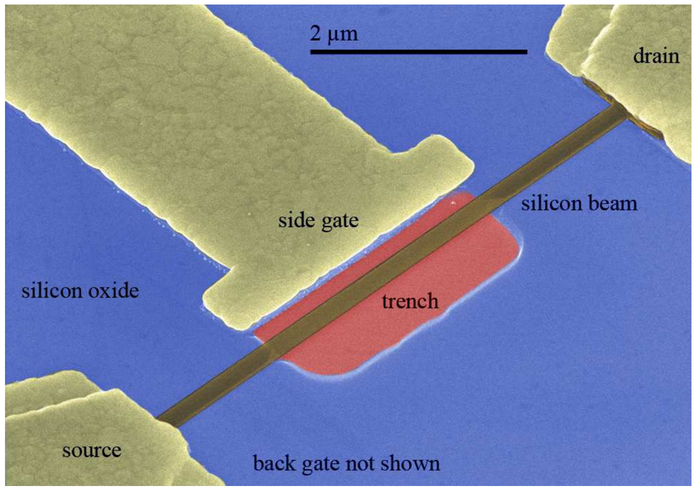

Figure 1.1. A false-color scanning electron microscope image of a representative device. Image from [14].

Figure 1.1 presents a false-color micrograph of the nanobeam system under consideration. The beam is etched out of a Silicon on Insulator (SoI) wafer, and suspended above a trench. The bottom substrate layer for this wafer serves as an electrode, or gate, which can electrostatically interact with the beam when a potential difference is applied between them. A second gate is also deposited to the left of the beam to provide the capability for in-plane excitation. The device was initially proposed and experimentally verified in [14], where more explicit detail on the fabrication processes can be found.

Nanobeams, such as that shown in Figure 1.1, are fundamentally coupled between the mechanical and electrical domains. As a result, their behavior needs to be studied from a system-level perspective which accounts for both domains. For example, the deflection of the beam inherently results in changes to the beam current and voltage and these changes then alter the forcing of the beam, which changes its deflection, and further changes the electrical state of the device. Effectively, the coupled domains lead to an internal feedback between the various transduction methods and the beam voltage. This feedback could introduce vibration in the beam beyond what is generated by the AC voltage components at the system inputs. Looking at anything but a system perspective of the device will not accurately capture these rich dynamics and will inaccurately predict the device's behavior.

One potential use of these systems is as electrical filters. The analysis, commentary and applications provided herein are primarily focused in this direction. The silicon nanobeams exhibit a mechanical resonance which occurs for only a narrow band of frequencies. The coupling between the electrical and mechanical domains correlates this to a narrow bandwidth of AC forcing frequencies which produce a resonant response. Furthermore, the use of these systems in a vacuum removes a large viscous damping force exerted by the air and leads to an increase in the resonant amplitude and a correspondingly smaller range of frequencies which fall into the 3 dB range below the resonant amplitude that is traditionally considered the pass-band of a filter. The quality factor of a filter is a measure of the relative bandwidth of the system [51], and has been shown to reach values as high as 2000 in similar beam resonators tested at low temperatures [4, 9], and much higher in other configurations [52]. In a linear system, the higher the quality factor, the narrower the bandwidth of the filter at a given resonant frequency. For certain applications a large quality factor, corresponding to a narrow bandwidth, is a highly desirable trait. For example, within a wireless communication network, the ability to create a narrower passband allows the use of more devices in a set frequency range.

CHAPTER 2. SYSTEM-LEVEL MODEL DEVELOPMENT

The model presented herein differentiates itself from prior work by approaching the description of the system output not merely as the displacement of the beam or the amplitude of the source current, but as a full description of the system. Prior models have been built using a variety of approximations for the beam's behavior. They range from treating the beam as a parallel plate [26, 53] to treating it as a continuous beam with midplane stretching and tension effects [47, 54]. Other works merely attempt to model the output current by investigating the electrical interaction between the beam and gate, and qualitatively compare this to experimental results [9, 34, 39]. In contrast, the model developed here seeks to combine the best of each of these efforts to form an appropriate system-level model that can predict both the beam response and the circuit response, while accounting for the interaction between them.

2.1 Mechanical Equation of Motion

Within the mechanical domain, the beam was analyzed as a standard fixed-fixed beam, despite several dimensions being only a hundred nanometers long. Prior work [35, 45, 55] shows that despite the small size, classical beam models can still provide accurate predictions of dynamic responses. Assuming that the shear throughout the beam is negligibly small, and that the beam is slender (that is, assuming $\sqrt{I/A}$ is small, where I is the moment of inertia and A is the area of the beam cross-section), an Euler-Bernoulli model of the beam was developed, which accounted for nonlinear mid-plane stretching. The ability to investigate the effects of any residual axial stresses remaining from fabrication, which were assumed to be constant throughout the beam, was also included. This led to the partial differential equation,

$$\begin{aligned}\rho wh\frac{\partial^2 y(x,t)}{\partial t^2}&+c\frac{\partial y(x,t)}{\partial t}+EI\frac{\partial^4 y(x,t)}{\partial x^4}\\&-\left\{S_r wh+\frac{Ewh}{2L}\int_0^L\left[\frac{\partial y(x,t)}{\partial x}\right]^2\mathrm{d}x\right\}\frac{\partial^2 y(x,t)}{\partial x^2}=F(x,t),\end{aligned}\tag{2.1}$$

where L, w and h are the length, width, and height of the beam, respectively, while ρ is the mass density and E is the modulus of elasticity for the material. S_r is the average, uniform, residual axial stress in the beam and $y(x,t)$ is the deflection of the beam at time t and at a distance along the beam, x. c is the specific viscous damping coefficient for the beam. While the etching processes used to release the beam results in a slight trapezoidal cross-section, it is sufficient to approximate the shape as the desired rectangular cross section. This results in a moment of inertia for out-of-plane motion of

$$I=\frac{1}{12}wh^3.\tag{2.2}$$

Figure 2.1 defines the positive direction for each of the relevant coordinates. It should be noted that while the devices were fabricated with the potential to be actuated both in- and out-of-plane, the model developed here accounts only for out-of-plane excitation from the back gate as a simplifying assumption. For information on the effects of the side gate's presence under this assumption, please refer to Section 3.1.

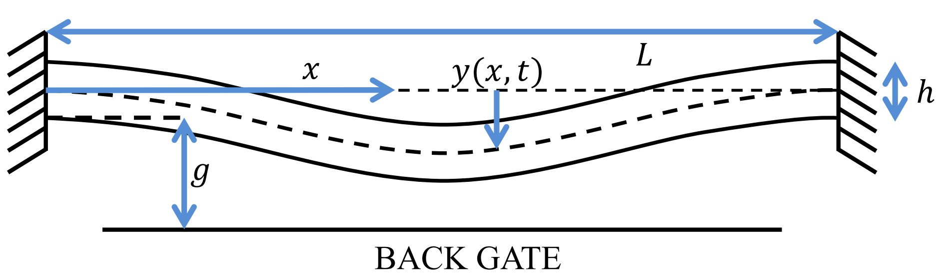

Figure 2.1. Beam variables for a back gate only excitation scenario. The electrostatic force acts between the bottom of the beam and the back gate when fringe fields are neglected.

If only small excitations near the first resonance of the beam are considered, then the equation can be simplified using the single-mode approximation,

$$y(x,t) = \phi(x)z(t). \tag{2.3}$$

The spatial definition of the first natural mode of the beam, $\phi(x)$, was developed using the single-mode approximation on the linear, unforced version of the beam equation. The final definition of $\phi(x)$ depends upon the boundary conditions selected for the beam. While it is clear from scanning electron micrographs (SEMs), such as Figure 2.2, that the fabrication of the devices can lead to undercutting of the beam ends and produce difficult-to-model boundary conditions, it is assumed that the boundary conditions for the beam can be approximated as ideally fixed on both ends. The true effects of the non-ideal boundary conditions are still under investigation, and beyond the scope of this work. More information on the effects of boundary conditions on damping can be found in [24] and [37].

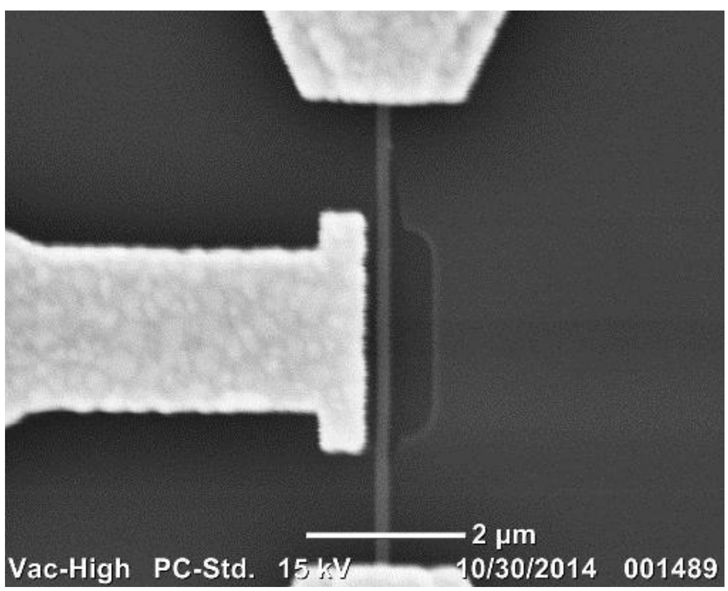

Figure 2.2. A scanning electron micrograph of a representative beam, showing a large undercut region below the top beam support. Photo Credit: Hossein Pajouhi.

The mode shape, $\phi(x)$ is normalized such that it becomes unity at the beam midpoint, $x = \frac{L}{2}$. This simplifies the understanding of $z(t)$ to be the deflection of the beam midpoint, and thus the maximum deflection of the beam in the case of the first natural mode of a fixed-fixed beam. Besides enabling an intuitive understanding, it also simplifies the description of the electrostatic forcing and capacitance models, which will be developed based upon the midpoint voltage of the beam in Section 2.2.

With a known mode shape, the partial differential equation can be discretized using Galerkin methods to obtain an ordinary differential equation in terms of $z(t)$,

$$\begin{aligned}
\rho w h & \int_0^L \phi^2(x)\,\mathrm{d}x\,\ddot{z}(t) + c\int_0^L \phi^2(x)\mathrm{d}x\,\dot{z}(t) \\
& + \left[EI\int_0^L \phi''''(x)\phi(x)\,\mathrm{d}x\; - S_r w h\int_0^L \phi''(x)\phi(x)\,\mathrm{d}x\right] z(t) \\
& - \frac{Ewh}{2L}\int_0^L \left[\phi'(x)\right]^2\,\mathrm{d}x\int_0^L \phi''(x)\phi(x)\,\mathrm{d}x\,z^3(t) \\
& = \int_0^L F(x,t)\phi(x)\,\mathrm{d}x,
\end{aligned} \tag{2.4}$$

where

$$(\bullet)' = \frac{\partial(\bullet)}{\partial x}, \qquad \dot{(\bullet)} = \frac{\partial(\bullet)}{\partial t}. \tag{2.5}$$

The damping that affects these beams is still a topic of research. Here a specific damping constant, c, is used as an approximation to capture the possible effects of both intrinsic and extrinsic damping from a wide variety of potential sources including, but not limited to, squeeze film damping, support loss, thermoelastic dissipation and phonon-phonon interactions. Various approximations exist throughout the literature [24, 25, 37, 38, 56, 57] for these effects. Viscous air damping, since it can be more easily controlled than other factors, is one of the most thoroughly understood. Reference [56] suggested that viscous damping for the devices presented here would be negligible for testing at low pressures (such as $< 75\,\mu$Torr, which was used for the experimental data presented herein).

2.2 Electrostatic Modeling

The usefulness of these NEMS devices arises from their electromechanical nature. The ability to develop an electric potential within the beam opens the door to a variety of interesting dynamic and electric effects beyond those associated with the purely-mechanical displacement of a beam. By applying a potential difference between the beam and a nearby electrode, also referred to as a gate, the beam is electrostatically attracted towards the gate, resulting in the distributed force present in Equations (2.1) and (2.4). At the same time, the beam-gate interaction forms a variable capacitor, allowing for a current flow between the two surfaces, and the piezoresistive properties of silicon result in a beam resistance that varies with the beam deflection. These effects combine to form a delicate interaction between the beam and its voltage, making a proper understanding of each interaction important.

2.2.1 Forcing Model

The potential difference between the beam and gate produces a distributed electrostatic force attracting the beam towards the gate. The force per unit length is dependant on the voltage of the beam and the distance between the two surfaces according to

$$F_{pp}(x,t) = \frac{\epsilon_0 w V_{gap}^2(x,t)}{[g - y(x,t)]^2}, \tag{2.6}$$

where $V_{gap}(x,t)$ is the instantaneous potential difference between the gate and the beam at some distance along the beam, x. Here g is the nominal gap size, and ϵ_0 is the permittivity of free space. For two surfaces with a uniform potential difference and a uniform gap, referred to as the parallel-plate model, this force can be easily represented. The physically-accurate model is complicated by the non-constant deflection along the beam and the internal resistance of the beam, which together lead to a different potential and deflection at every point along the beam. Despite this, it is not uncommon to utilize the parallel-plate description to approximate the beam's behavior by neglecting any curvature in the beam deflection and assuming that the entire beam is at a single voltage [18, 26, 39, 54]. Several theoretical studies have investigated better approximations to more fully capture the dynamics of the situation, often utilizing finite element analyses to support their theory. For example, Reference [18] demonstrates the shortcomings of the parallel-plate model when considering a large beam curvature and proposes several expanded models to account for the beam's mode shape. Instead of focusing on the beam curvature, Reference [58] proposes an improved capacitance model, which relates to the electrostatic forcing through

$$F = \frac{1}{2} V_{gap}^2 \frac{\partial C}{\partial y}, \tag{2.7}$$

by including fringing field corrections to account for the electric field behavior around the finite cross-section of the nanobeam. Both methods greatly improve the accuracy of the model compared to the basic parallel-plate approximation. Specifically, the models presented in [58] are shown to improve the estimation of the pull-in voltage.

Since the pull-in voltage was not of primary concern for this work, the forcing model to use in the system-level description was selected from those presented in [18]. The model which most accurately matched the finite element analysis presented there was a 4^{th}-order perturbation of the spatial function describing the potential between the beam and the gate. Because Equation (2.4) requires the integral of the forcing function with respect to x, the forcing model presented in [18] was expanded in a Taylor series about $z(t) = 0$, keeping terms up to $z^3(t)$, after substituting Equation (2.3). This produces a forcing definition with no function of x in the denominator, while enforcing the same order of accuracy as in Equation (2.1). This approach inherently limits all analysis to small deflections of the beam [$z(t)$ near zero]. It also indicates that the model will not accurately predict pull-in effects, as the forcing model loses the singularity that occurs in the exact solution when $z(t)$ approaches the gap size, g. The final representation of the forcing,

$$\begin{aligned} F_{P4}(x,t) \approx & \frac{\epsilon_0 w V_{gap}^2(t)}{90 g^5} \left(45g^3 + \left\{90\phi(x) - 2g^2\left[15\phi''(x) + g^2\phi''''(x)\right]\right\} g^2 z(t)\right. \\ & + \left\{135g\phi^2(x) + g^3\left[-15\phi'^2(x) + 3g^2\phi''^2(x) + 4g^2\phi'''(x)\phi'(x)\right]\right. \\ & \quad \left. +2g^3\left[-15\phi''(x)\phi(x) + g^2\phi''''(x)\phi(x)\right]\right\} z^2(t) \\ & + \left[180g\phi^3(x) - 30g^2\phi'^2(x)\phi(x) - 30g^2\phi''(x)\phi^2(x)\right. \\ & \quad \left.\left. +48g^4\phi''(x)\phi'^2(x)\right] z^3(t)\right), \end{aligned} \tag{2.8}$$

is proportional to $V_{gap}^2(t)$, which produces a mixing effect when harmonic voltages are applied to the beam and/or gate.

It should be noted that the model presented here, and indeed most of the models presented throughout the literature [18,34,48,59,60], assume a uniform voltage along the beam. It is apparent from the finite element analysis in [18] that this is not an excessive hindrance to the accuracy of the model. Throughout this thesis, $V(t)$ can be assumed to represent the voltage at the midpoint of the beam, which will be used as a representative voltage for the entire beam. Similarly, $V_b(t)$ will represent the back gate voltage, such that

$$V_{gap}(t) = V_b(t) - V(t). \tag{2.9}$$

This notation also assists with the definition of the capacitance and piezoresistance in the following sections. The dependence of the forcing on both the potential difference between the beam and gate, as well as the beam's deflection, manifests in an ability to electrostatically tune the resonant frequency. This effect can be more clearly seen from the equations in Section 2.4 and will be explored in Section 4.1.

2.2.2 Capacitance Model

As highlighted in Equation (2.7), the electrostatic forcing and the capacitance of the beam-gate system are directly related. Therefore, it is important that both are described with similar accuracy. Therefore, the capacitance model is again taken from [18], and carries the same advantages as the selected forcing model. That is, the model accounts for large beam curvatures, but approximates the distributed voltage with the midpoint voltage and neglects fringing field effects. The capacitance equation developed from the forcing model is initially in the form of $\frac{\partial C}{\partial x}$. Similar to the forcing equation, Equation (2.8), this capacitance description is expanded in a Taylor series around $z(t) = 0$, keeping terms up to $z^3(t)$. It is then integrated along the length of the beam to provide the average capacitance,

$$C(t) = \frac{\epsilon_0 L}{g}\left[L + k_1 z(t) + k_2 z^2(t) + k_3 z^3(t)\right], \tag{2.10}$$

where the geometric parameters k_1 through k_3 are defined in Table 2.1. The dependence of the capacitance upon the beam displacement means that the standard description of the current flow through a capacitor does not apply in this case. Beginning instead with the general definition of the charge present in a capacitor,

$$Q(t) = V_{gap}(t)C(t), \tag{2.11}$$

along with the general definition of current,

$$i(t) = \frac{\mathrm{d}Q}{\mathrm{d}t}, \tag{2.12}$$

the product rule of differentiation shows that the current flow between the beam and a gate is defined as

$$i_{cap}(t) = \dot{C}(t)V_{gap}(t) + C(t)\dot{V}_{gap}(t). \tag{2.13}$$

Here, $Q(t)$ is the charge build-up in the capacitor. The variable capacitance allows for a purely-DC loaded capacitor to generate a current flow between the beam and gate as the beam deflects. The dependence of the current upon $\dot{C}(t)$ is truly a dependence upon $\dot{z}(t)$, and while the beam displacement may always be very small, it is possible for the beam velocity to be much larger, and produce a current that can in turn produce noticeable contributions to the overall output current.

Note from Equations (2.1) and (2.8) that $z(t)$ will be proportional to $V_{gap}^2(t)$. Equation (2.10) then suggests that $C(t)$ will be proportional to $V_{gap}^6(t)$. The current equation, Equation (2.13), then reintroduces the gap voltage such that $i_{cap}(t)$ will be proportional to $V_{gap}^7(t)$. The harmonic mixing terms in the electrical output are therefore significant and will be explored further in Section 3.2 and Chapter 5.

2.2.3 Piezoresistive Effects

Silicon has been shown to exhibit an electrical dependence upon strain, known as piezoresistivity. These properties of silicon were thoroughly described by Kanda in [61], and have been experimentally verified throughout literature [46, 62]. Strains both parallel and perpendicular to the current flow can affect the resistance observed by the circuit. The strains in a beam due to linear deflections are equal and opposite on either side of the neutral axis, which results in a net zero strain in any instantaneous cross section and no net resistivity change [41]. However, mid-plane stretching implies a lengthening of the neutral axis and a strain induced uniformly across a cross-section of the beam, resulting in a net change in the resistivity. Therefore, in order to determine the instantaneous resistance of the beam, the strain due to mid-plane stretching must be determined. While this strain is typically small, the piezoresistive coefficients in silicon can be large enough to ensure that piezoresistivity is a relevant transduction mechanism.

As described in [41], the axial strain from mid-plane stretching, ϵ, can be shown to be

$$\epsilon(t) = \frac{1}{2L} \int_0^L \left[\frac{\partial y(x,t)}{\partial x} \right]^2 \mathrm{d}x. \tag{2.14}$$

For a fixed-fixed beam and assuming the first natural mode shape, Reference [41] shows Equation (2.14) to simplify to

$$\epsilon(t) = 2.44 \left[\frac{z(t)}{L} \right]^2 . \tag{2.15}$$

This approximation was verified by a numerical comparison to the strain model presented in [54], which derives a strain equation by analyzing the transverse and axial strains arising during deflection. The different approaches were found to be in excellent agreement. The dependence of the strain on the square of the displacement captures the fact that the beam undergoes two periods of strain for every period of beam deflection, as expected. The strain from midplane stretching develops only an axial strain, and therefore the transverse and shear stresses can be assumed to be negligible, leading to the beam resistance equation,

$$R_{beam}(t) = R_0 \left[1 + \epsilon(t) G_R\right], \tag{2.16}$$

where R_0 is the nominal beam resistance given by

$$R_0 = \frac{\rho_r L}{wh}. \tag{2.17}$$

Here, ρ_r is the nominal resistivity of the doped silicon. G_R in Equation (2.16) is the resistance gauge factor,

$$G_R = 1 + 2\nu + E\pi_L. \tag{2.18}$$

This gauge factor captures both geometric effects, represented by $(1+2\nu)$, where ν is Poisson's ratio for the beam material, and piezoresitive effects, encompassed by $E\pi_L$. Here, π_L is the effective longitudinal piezoresistive coefficient, which introduces the dependence of the piezoresistive effect on crystal orientation and other parameters, such as doping and temperature [61]. The crystal structure of silicon, and the direction of the current flow with respect to the crystal lattice, have a significant effect on the piezoresistive variations observed. In some orientations, [61] shows near-unity piezoresistive coefficents, which implies a resistive change on the same order as the strain, which will lead to negligible resistance fluctations. In other configurations, works such as [46] have shown large piezoresistive coefficents which can produce measurable currents from a small strain. Reference [61] contains the information necessary to determine proper π_L values for a unique orientation, doping level and temperature for single-crystal silicon. In [46], He and Yang show the effective piezoresistive coefficients in silicon nanowires to be highly dependent upon the diameter of the nanowires in addition to the aforementioned parameters. They show that the piezoresistive effect is greatly amplified by having smaller diameter nanowires as compared to the piezoresistive effects in bulk silicon. The exact nature and magnitude of a size effect on a silicon nanobeam of the size under investigation here has yet to be studied. Therefore, the piezoresistive effects present in the nanobeams were assumed to be the same as those found in bulk silicon. It should also be noted that the assumption to consider only axial strain will still hold if both the side gate and back gate are implemented, but the approximation for the strain in the beam becomes significantly more complex as both degrees of freedom are considered.

The final representation of the beam resistance,

$$R_{beam}(t) = \frac{\rho_r L}{wh}\left\{1 + 2.44\left[\frac{z(t)}{L}\right]^2 (1 + 2\nu + E\pi_L)\right\}, \tag{2.19}$$

clearly shows the dependence of the beam resistance on $z^2(t)$. As described in Section 2.2.2, the dependence of $z(t)$ on $V_{gap}^2(t)$ implies that the fluctuations in resistance will be related to $V_{gap}^4(t)$.

It is rare to find literature describing a MEMS or NEMS device that considers both capacitance modulation and piezoresistive effects simultaneously. The dearth of models analyzing such a system is rooted in the typical device designs. In the majority of work involving silicon nanobeams, it is not the current through the beam that is monitored, rather a current flow from a gate to the beam, and often on to another sensing gate, as is done in [13, 34, 51]. In these cases, the lack of current flowing along the length of the beam provides no opportunity for piezoresistive effects to modulate the current, since the axial strain is perpendicular to the current flow, which leads to a small piezoresistive effect. Some devices do measure the current flow along a beam, but in these cases they are either mechanically actuated, such that a piezoresistive, or similar, measurement is all that is available [41, 46], or they are fabricated from carbon nanotubes and other materials with different piezoresistive properties [9,39,45]. Other systems focus primarily on the piezoresistive outputs that arise from external strain gauges that are attached to the beam, but do not consist of the entirety of the beam [63, 64], and thereby ignore currents from capacitive effects. That said, it is not unheard of to combine the two effects, as Grogg and Ionescu do so in their work on the vibrating body transistor [6].

2.3 System-Level Circuit Representation

With a basic understanding of the transduction mechanisms at work in these systems, a representative circuit diagram can be developed in order to clearly relate the electrical system inputs to the mechanical motion and electrical outputs. As developed in Section 2.2.2, the interaction between the beam and gate can be defined as a variable capacitor dependent on the potential difference between the gate and the beam midpoint. Section 2.2.3 then describes the beam as a variable resistor, whose resistance is dependent upon the beam deflection. To combine these two concepts, the effective resistance of the beam is split into two halves, in order to properly model the midpoint voltage's interaction with the gate. Figure 2.3 demonstrates this circuit representation.

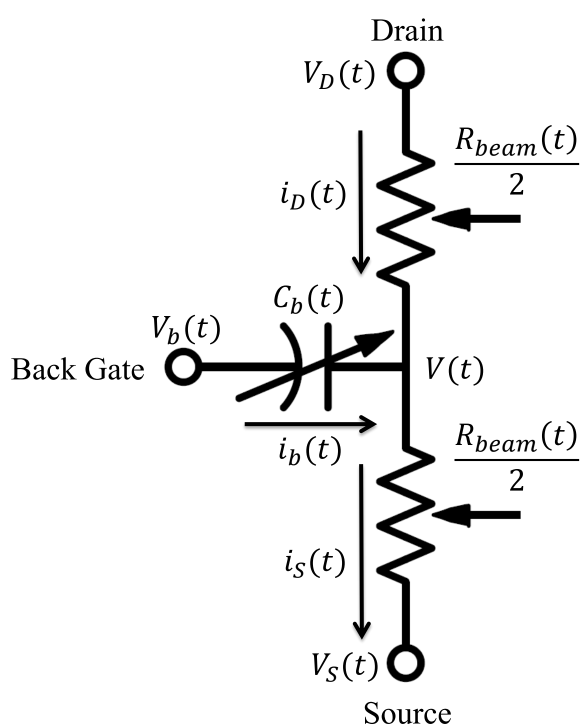

Figure 2.3. An effective circuit representation of the nanobeam with a single gate. The arrows define the direction of positive current flows.

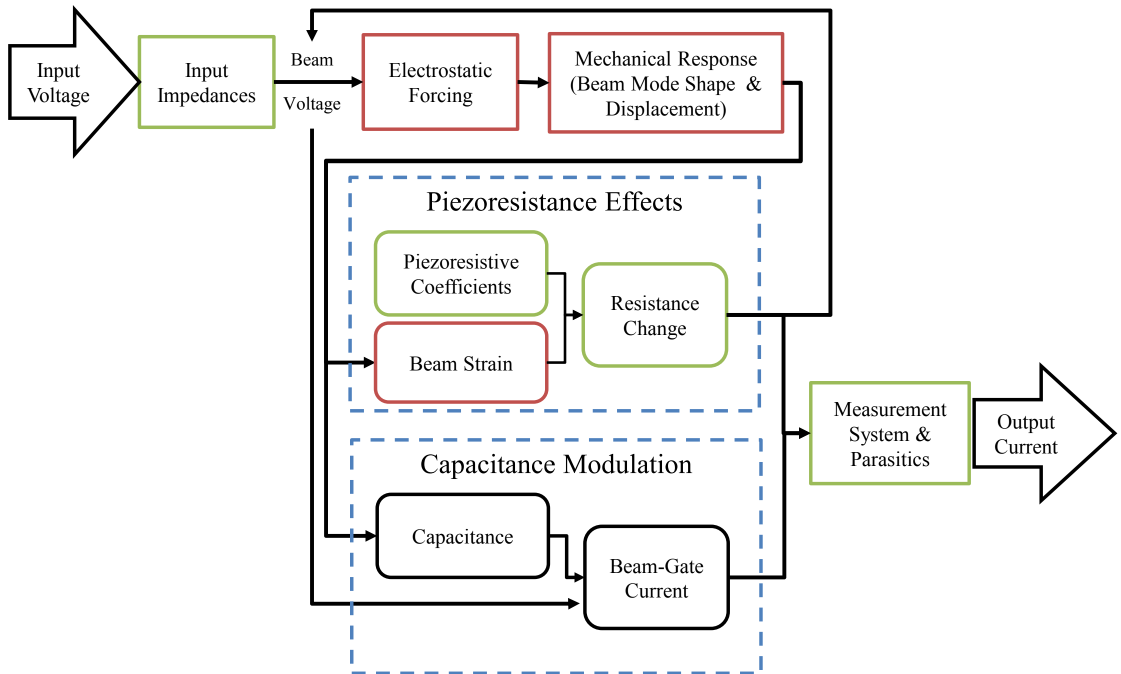

Figure 2.4. A block diagram of the various interactions occurring between the input voltage and output current for the system, including associated excitation and measurement circuits.

Figure 2.4 charts the system interactions and assists in visualizing the complexity of the interactions occurring during the device's operation. The interaction between the capacitive effects and the piezoresistive effects and their influence on the beam displacement, and thus forcing, produces rich dynamics and what can be thought of as a natural feedback loop internal to the system.

Kirchhoff's current law can be used to develop an equation to describe the electrical interactions of the circuit mathematically. Given the currents of Figure 2.3, and summing at the 'node' representing the beam midpoint gives,

$$i_D(t) + i_b(t) = i_S(t). \tag{2.20}$$

Substituting Equation (2.13) for $i_b(t)$ while using Ohm's law for $i_D(t)$ and $i_S(t)$ and grouping the resistive terms together reveals that

$$\frac{2[V(t) - V_S(t)]}{R_{beam}(t)} - \frac{2[V_D(t) - V(t)]}{R_{beam}(t)} = \dot{C}_b(t)[V_b(t) - V(t)] + C_b(t)[\dot{V}_b(t) - \dot{V}(t)]. \tag{2.21}$$

Expanding the capacitance [Equation (2.10)] and resistance [Equation (2.19)] further,

$$\frac{2[2V(t) - V_D(t) - V_S(t)]}{k_0 R_0 \left[1 + P_r z^2(t)\right]} = \left[k_1 + 2k_2 z(t) + 3k_3 z^2(t)\right] \dot{z}(t) \left[V_b(t) - V(t)\right] + \left[L + k_1 z(t) + k_2 z^2(t) + k_3 z^3(t)\right] \left[\dot{V}_b(t) - \dot{V}(t)\right], \quad (2.22)$$

reveals a definition for the beam midpoint voltage and deflection in terms of the circuit inputs, $V_b(t)$, $V_D(t)$, and $V_S(t)$. The piezoresistive effects are represented here as $P_r = 2.44\frac{G_r}{L^2}$. Equations (2.4) and (2.8) can be combined to reveal the full beam equation of motion,

$$B_0 \ddot{z}(t) + B_1 \dot{z}(t) + \left\{B_2 - \alpha f_1 \left[V_b(t) - V(t)\right]^2\right\} z(t) - \alpha f_2 \left[V_b(t) - V(t)\right]^2 z^2(t) - \left\{B_3 + \alpha f_3 \left[V_b(t) - V(t)\right]^2\right\} z^3(t) - \alpha f_0 \left[V_b(t) - V(t)\right]^2 = 0, \quad (2.23)$$

which, along with Equation (2.22), presents a system of equations describing the full behavior of a single-gate resonator system. The coefficients in Equations (2.22) and (2.23) can be found in Table 2.1. The beam equation maintains a near Duffing-like form, with the exception of the electrostatic terms, which softens the linear stiffness while also contributing quadratic and cubic nonlinearities.

It should be noted that while this set of equations represents a single-gate operation, and while the experimentation discussed in Chapter 3 considers only forcing through the back gate, it was determined that the presence of the side gate is non-negligible in the practical operation of the device. It was experimentally shown that several of the devices had measurable resistances between the back and side gates, and therefore when a potential is applied to one, it affects both gates. Due to the increased gap size for the side gate (200 nm, as opposed to 144 nm for the back gate) on the devices tested, and the drop in potential due to the resistance between the gates, it is appropriate to presume that the leakage to the side gate will not result in any forcing of the beam. Therefore, in the cases where the side gate must be considered it is presented as a static capacitor acting between the gate and the beam. This representation is included in Figure 3.2, along with other circuit representations of wafer level effects discussed in Section 3.1.

Table 2.1. Coefficients - Dimensional Form.

Coefficient	Expression
B_0	$\rho A \int_0^L \phi^2 \, \mathrm{d}x$
B_1	$c \int_0^L \phi^2 \, \mathrm{d}x$
B_2	$EI_b \int_0^L \phi'''' \phi \, \mathrm{d}x - S_r w h \int_0^L \phi'' \phi \, \mathrm{d}x$
B_3	$\frac{EA}{2L} \int_0^L \phi'^2 \, \mathrm{d}x \int_0^L \phi'' \phi \, \mathrm{d}x$
f_0	$45 g^3 \int_0^L \phi \, \mathrm{d}x$
f_1	$g^2 \left[90 \int_0^L \phi^2 \, \mathrm{d}x - 2g^2 \left(15 \int_0^L \phi'' \phi \, \mathrm{d}x + g^2 \int_0^L \phi'''' \phi \, \mathrm{d}x \right) \right]$
f_2	$135 g \int_0^L \phi^3 \, \mathrm{d}x + g^3 \left(-15 \int_0^L \phi'^2 \phi \, \mathrm{d}x + 3g^2 \int_0^L \phi''^2 \phi \, \mathrm{d}x + 4g^2 \int_0^L \phi''' \phi' \phi \, \mathrm{d}x \right)$ $+ 2g^3 \left(-15 \int_0^L \phi'' \phi^2 \, \mathrm{d}x + g^2 \int_0^L \phi'''' \phi^2 \, \mathrm{d}x \right)$
f_3	$180 \int_0^L \phi^4 \, \mathrm{d}x - 30 g^2 \int_0^L \phi'^2 \phi^2 \, \mathrm{d}x - 30 g^2 \int_0^L \phi'' \phi^3 \, \mathrm{d}x + 48 g^4 \int_0^L \phi'' \phi'^2 \phi \, \mathrm{d}x$
f_c	$\frac{\epsilon_0 w V^2(t)}{90 g^5}$
κ_1	$\frac{1}{g} \int_0^L \phi \, \mathrm{d}x$
κ_2	$\frac{1}{g^2} \int_0^L \phi^2 \, \mathrm{d}x + \frac{1}{3} \int_0^L \phi'^2 \, \mathrm{d}x + \frac{g^2}{45} \left(\int_0^L \phi''^2 \, \mathrm{d}x + 2 \int_0^L \phi''' \phi' \, \mathrm{d}x \right)$
κ_3	$\frac{1}{45 g^3} \left(45 \int_0^L \phi^3 \, \mathrm{d}x + 6 g^4 \int_0^L \phi'' \phi'^2 \, \mathrm{d}x + 15 g^2 \int_0^L \phi'^2 \phi \, \mathrm{d}x \right.$ $\left. - g^4 \int_0^L \phi''^2 \phi \, \mathrm{d}x - 2 g^4 \int_0^L \phi''' \phi' \phi \, \mathrm{d}x \right)$

2.4 Nondimensionalized System Model

In order to better identify the impact that geometric and other design changes have on the system behavior, the primary equations were normalized. This process led to a variety of nondimensional terms, providing a reduction from the initial number of system variables. Initially normalizing the independent variables, x and t, with respect to the beam length, L, and the period of the linear beam's first natural resonance, gives

$$\hat{x} = \frac{x}{L}, \tag{2.24}$$

$$\hat{t} = \omega_n t = \omega_0 \sqrt{\frac{Eh^2}{12\rho L^4}}\, t. \tag{2.25}$$

Note that $\hat{t}$ assumes a square cross-sectional area for the beam. These definitions change the behavior of the derivatives and integrals such that,

$$(\bullet)' = \frac{\partial(\bullet)}{\partial x} = \frac{1}{L}\frac{\partial(\bullet)}{\partial \hat{x}} \tag{2.26}$$

$$\int_0^L (\bullet)\, \mathrm{d}x = L \int_0^1 (\bullet)\, \mathrm{d}\hat{x} \tag{2.27}$$

$$\dot{(\bullet)} = \frac{\partial(\bullet)}{\partial t} = \frac{1}{\omega_n}\frac{\partial(\bullet)}{\partial \hat{t}} = \frac{1}{\omega_0}\sqrt{\frac{12\rho L^4}{Eh^2}}\frac{\partial(\bullet)}{\partial \hat{t}}. \tag{2.28}$$

The mode shape of the beam deflection, $\phi(x)$, can now be redefined as

$$\phi(x) = \phi(\hat{x}L) = \hat{\phi}(\hat{x}). \tag{2.29}$$

The midpoint deflection, $z(t)$ was normalized to be

$$\hat{z} = \frac{z}{g}, \tag{2.30}$$

such that $\hat{z} = 1$ represents a beam deflected the full range of the gap. Any voltages may be normalized using the linear estimate of the static pull-in voltage,

$$\hat{V} = \frac{3}{32}\sqrt{\frac{12\epsilon_0 L^4}{Eh^3 g^3}}\, V. \tag{2.31}$$

Implementing these normalizations with Equations (2.22) and (2.23) leads to the emergence of several other nondimensional parameters, summarized in Table 2.2. Substituting these parameters into Equations (2.22) and (2.23) and simplifying results in a system of three first-order differential equations in state space by defining

$$y_1(\hat{t}) = \hat{z}(\hat{t}), \tag{2.32}$$

$$y_2(\hat{t}) = \dot{\hat{z}}(\hat{t}), \tag{2.33}$$

$$y_3(\hat{t}) = \hat{V}(\hat{t}), \tag{2.34}$$

leads to a system of differential equations which can be written as

$$\dot{y}_1(\hat{t}) = y_2(\hat{t}), \tag{2.35}$$

$$\begin{aligned}\dot{y}_2(\hat{t}) = \beta y_2(\hat{t}) &+ \left\{\alpha_{10} + \alpha_{11}\left[\hat{V}_b(\hat{t}) - y_3(\hat{t})\right]^2\right\} y_1(\hat{t}) + \alpha_2\left[\hat{V}_b(\hat{t}) - y_3(\hat{t})\right]^2 y_1^2(\hat{t}) \\ &+ \left\{\alpha_{30} + \alpha_{31}\left[\hat{V}_b(\hat{t}) - y_3(\hat{t})\right]^2\right\} y_1^3(\hat{t}) + \alpha_0\left[\hat{V}_b(\hat{t}) - y_3(\hat{t})\right]^2,\end{aligned} \tag{2.36}$$

$$\dot{y}_3(\hat{t}) = \frac{N}{D} + \frac{\dot{\hat{V}}_b(\hat{t})}{\kappa}. \tag{2.37}$$

$$\begin{aligned}N = \psi\left[\hat{V}_D(\hat{t}) + \hat{V}_S(\hat{t})\right] - \eta_{00}y_3(\hat{t}) + \left[\hat{V}_b(\hat{t}) - y_3(\hat{t})\right] y_2(\hat{t})\Big[\eta_0 + \eta_1 y_1(\hat{t}) \\ + \eta_2 y_1^2(\hat{t}) + \eta_3 y_1^3(\hat{t}) + \eta_4 y_1^4(\hat{t})\Big]\end{aligned}$$

$$D = \kappa\left[\gamma_0 + \gamma_1 y_1(\hat{t}) + \gamma_2 y_1^2(\hat{t}) + \gamma_3 y_1^3(\hat{t}) + \gamma_4 y_1^4(\hat{t}) + \gamma_5 y_1^5(\hat{t})\right]$$

The corresponding coefficients are tabulated in Tables 2.3 and 2.4. Note that the presented values are specifically for the single mode under consideration. Therefore, the mode shape integrals and the nondimensional coefficient $\hat{m}$ have already been assigned values in Tables 2.3 and 2.4.

These equations clearly give evidence of the voltage's effects with regards to softening the linear, and cubic, stiffness of the beam. It also provides a direct contribution to the beam acceleration. The dependence of the voltage on the beam position is complex, raising difficulties in developing immediate inituition for the system's behavior. Since the circuit portion of the system of equations, $\dot{y}_3(t)$, is only a first-order differential equation, it does not contribute its own resonant dynamics. Therefore the system will still exhibit primarily Duffing-like responses, but the exact shape and tuning of the resonances will vary due to more complex beam-voltage interactions.

Table 2.2. Nondimensional Parameters.

Parameter	Expression	Description
$\hat{x}$	$\frac{x}{L}$	Ratio of position along beam to beam length
$\hat{t}$	$\omega_0\sqrt{\frac{Eh^2}{12\rho L^4}}t$	Nondimensional time
$\hat{\phi}(\hat{x})$	$\phi(x)$	Beam mode shape
$\hat{z}$	$\frac{z}{g}$	Ratio of midpoint deflection through the gap
$\hat{V}$	$\frac{3}{32}\sqrt{\frac{12\epsilon_0 L^4}{Eh^3g^3}}V$	Ratio of voltage to static pull-in
$\hat{L}$	$\frac{L}{g}$	Effective aspect ratio of the system
$\hat{g}$	$12\left(\frac{g}{h}\right)^2$	Ratio of gap size to beam height
$\hat{c}$	$\frac{12c^2L^4}{E\rho w^2h^4}$	Nondimensional damping
$\hat{s}$	$\frac{12L^2S_r}{E}$	Nondimensional residual stress
$\hat{\rho}_r$	$\epsilon_0\rho_r\sqrt{\frac{E}{12w^2\rho}}$	Capacitance and piezoresistance coupling
$\hat{m}$	ω_0^2	Mode scaling factor
$\hat{\omega}$	$\frac{\omega}{\omega_0\sqrt{\frac{Eh^2}{12\rho L^4}}}$	Ratio of frequency to linear resonant frequency

Table 2.3. Coefficients - Nondimensional Form.

Coefficient	Expression
β	$-0.0446\sqrt{\hat{c}}$
α_0	0.1496
α_{10}	$-(0.9976 + 0.0245\hat{s})$
α_{11}	$0.2268 + \dfrac{0.9299}{\hat{L}^2} - \dfrac{2.5224}{\hat{L}^4}$
α_2	$0.2847 + \dfrac{0.6832}{\hat{L}^2} + \dfrac{1.5835}{\hat{L}^4}$
α_{30}	$-0.0598\hat{g}$
α_{31}	$0.3330 + \dfrac{0.5637}{\hat{L}^2} - \dfrac{3.5547}{\hat{L}^4}$
ψ	64
η_{00}	128
η_0	$11.7194\hat{\rho}_r\hat{L}$
η_1	$22.3014\dfrac{\hat{\rho}_r}{\hat{L}^5}(4.5188E{-}5\hat{L}^2 + 3.2661\hat{L}^4 + 0.7964\hat{L}^6)$
η_2	$22.3014\dfrac{\hat{\rho}_r}{\hat{L}^5}(5.56182\hat{L}^2 + (2.3997 + 1.2815G_r)\hat{L}^4 + \hat{L}^6)$
η_3	$22.3014\dfrac{\hat{\rho}_r G_r}{\hat{L}^5}(1.1021E{-}4 + 7.9654\hat{L}^2 + 1.94238\hat{L}^4)$
η_4	$22.3014\dfrac{\hat{\rho}_r G_r}{\hat{L}^5}(13.5644 + 5.8524\hat{L}^2 + 2.4388\hat{L}^4)$

2.5 Limitations of the Model

In order to condense the system into three ordinary differential equations, a variety of assumptions were made which place restrictions on the conditions under which the results of this model may be trusted. Primarily, only the first eigenmode of

Table 2.4. Coefficients - Nondimensional Form. Continued

Coefficient	Expression
γ_0	$3.0132\hat{L}^6$
γ_1	$1.5764\hat{L}^6$
γ_2	$-13.2888\hat{L}^2 + (4.8991 + 7.3486G_r)\hat{L}^4 + 1.1947\hat{L}^6$
γ_3	$5.5618\hat{L}^2 + (2.3997 + 3.8446G_r)\hat{L}^4 + \hat{L}^6$
γ_4	$(-32.4092 + 11.9481\hat{L}^2 + 2.9136\hat{L}^4)G_r$
γ_5	$(13.5644 + 5.8524\hat{L}^2 + 2.4388\hat{L}^4)G_r$
κ	$237.89\dfrac{\hat{\rho}_r}{\hat{L}^5}$

a fixed-fixed beam is represented in the final form of the equations, although they could be easily adapted for any other single eigenmode. The excitation for the beam cannot lead to situations which would normally require the expression of multiple mode shapes. Included in this prohibition is excitation far from any eigenfrequency of the beam since this will naturally lead to vibration in different mode shapes, which this model will misrepresent. Large amplitude beam deflections, such as a beam approaching pull-in, are also likely to require higher-order nonlinearities to accurately represent and therefore should be avoided. Because the modeled mode shape assumes an initially straight beam, the actual voltage required for pull-in is likely to be overestimated by the numerical coefficients presented in Tables 2.3 and 2.4. Similarly, the true midplane stretching strain will also have some non-zero offset corresponding to a different nominal resistance. These issues could be addressed developing a more detailed description of $\phi(x)$ for the coefficients in Table 2.1; however, the more complicated the mode shape, the more expensive the computation of the modeled response becomes.

Several steps in the model development required a Taylor series expansion around $z(t) = 0$ and kept only up to third-order terms, which further restricts the model to only small beam displacements. Therefore, the model is only advised for use with small excitations. The lack of higher-order terms may lead to a slight misrepresentation of the resonance shape, but for small beam displacements these discrepancies should be negligible. However, in order to study the true transient behavior or pull-in behavior of the beam, higher-order terms would be required. Further approximations, such as the damping model used, neglected fringe fields, and the use of the midpoint voltage for the forcing and capacitance calculations will result in slight variations from the physical reality, but for the small displacements under consideration the losses will be negligible. Practically speaking, the piezoresistive dependence upon crystal orientation implies that the results presented in the following sections are only truly valid for a system with the same crystal orientation as that described in Section 2.2.3.

These limitations, especially those related to the mode shapes represented, have interesting implications towards using the model to look at the response for frequency components affected and/or produced through the nonlinearities present in the beam forcing and electrical equations (see Section 3.2 for a more detailed exposition of this phenomena). While the primary frequency component may excite only a single mode shape, the secondary frequency components may need other eigenmodes to properly represent their response. However, since these secondary frequency components are extremely small, it is a safe assumption to presume that the eigenmode associated with the primary excitation will remain dominant and control the response.

CHAPTER 3. EXPERIMENTAL MODELING AND RESULTS

In order to confirm the accuracy and relevance of the model, experimental characterizations were completed, following the process previously developed for this class of devices in [14]. The testing methodology utilizes signal mixing to avoid the parasitics and test equipment limitations present in the megaHertz range, where the resonant frequency is located for typical devices. The nanobeams are electrically connected through a physical probe contact to metal pads deposited and attached to the beams during fabrication, as shown in Figure 3.1. The external circuitry, such as sources and filters, is also included in an overarching system-level model to predict the true response of the device to the system inputs. There are also several circuit elements added to the system in order to represent the parasitics and non-ideal performance of the wafer and probes.

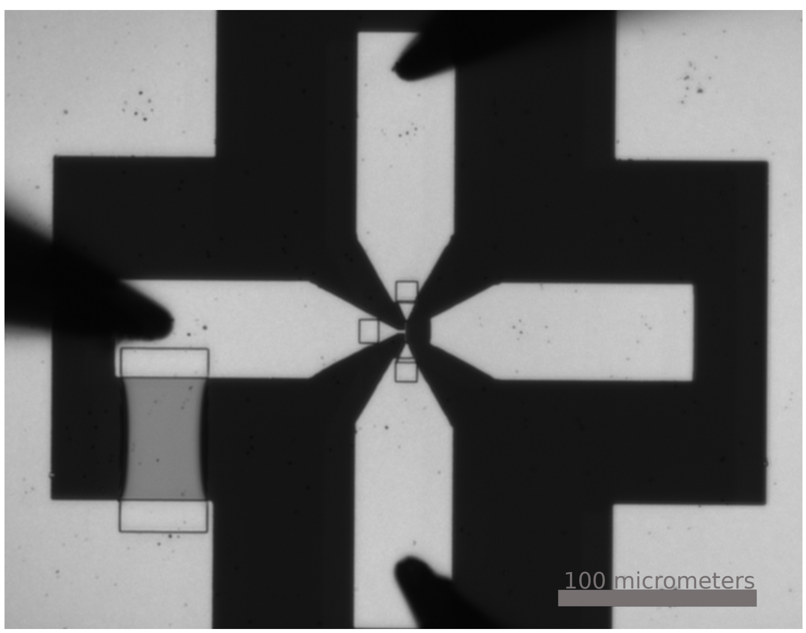

Figure 3.1. Optical microscope image (20x magnification) of the device pads and probe tips.

3.1 Experimental Setup

Though the model developed in Chapter 2 may provide the most relevant dynamics for an isolated, ideal nanobeam, it is only a subset of a full experimental test system. The full experimental setup is represented in Figure 3.2 and was fully described in [14]. For actuation, an amplitude-modulated AC signal was applied to the beam through the drain pad while a DC bias is applied to the back gate (see Figure 3.1). The resulting current through the beam was measured by a lock-in amplifier at the modulation frequency, f_m, which is produced in the output current by the nonlinearities in the electrostatic forcing and other electromechanical interactions (see Section 2.2). A typical experimental test consisted of slowly increasing or decreasing the carrier frequency of the modulated signal and recording the resulting amplitude and phase profile for the modulation frequency, which will be referred to as obtaining the up or down frequency sweep for the remainder of this thesis. The required signal sources, measurement systems and other parasitics must be considered in the model to achieve an accurate comparison to experimental results. The schematic in Figure 3.2 was developed to represent these interactions. Note that the inclusion of the aforementioned subsystems implies that the voltages forcing the beam are not the direct inputs applied to the system. Rather, the steady-state input to the beam will be attenuated and have additional frequency components arising from the beam nonlinearities.

Beyond those beam related dynamics presented in Chapter 2, there are several wafer-level effects which were determined experimentally and are included here to paint a full picture of the circuit under test. Due to the device substrate failing to provide proper insulation between the source and drain pads, a resistance R_{subs}, was included to model the possibility of currents bypassing the beam to contribute a direct feed-through current to the final output. Regrettably, a resistance measurement of a device between the source and drain reveals the combined resistance of the beam and substrate, so a unique identification of the substrate resistance was not directly obtainable. Several devices experienced some amount of finite resistance, and hence the electrical coupling, between the side and back gates, represented in Figure 3.2 as R_g. This leakage path prohibits the idea of performing a pure single-gate excitation test, even when a gate is left floating as the side gate is in Figure 3.2. Note that grounding the side gate would create a pathway to ground for the back gate bias, eliminating the bias' effect on the forcing of the beam.

The probes (American Probe & Technologies 72T series, 7 μm radius tip) and pads at the source and drain were also close enough to introduce a capacitive bypass of the beam, C_{pads}. Similar to the substrate resistance, but frequency dependent, this created a parallel path for current to bypass the beam. The value of this capacitance was estimated by assuming the probe tips were parallel plates placed at the ends of the source and drain pads. It was also experimentally estimated by raising the probes directly above the contact pads and looking at the response between the probes.

The measurement system also exhibited several parasitics affecting the final output. The contact of the probes with the pads on the device resulted in a contact resistance, R_C, for every connection made. While the back gate was excited through the bottom of the substrate, the contact with the probe station chuck was imperfect and featured a similar resistance. Unfortunately, since the exact resistances of the device components are unknown, the contact resistances can only be experimentally estimated with low fidelity. Because of the small size of the contact resistances in relation to the device resistance, it was assumed that a single average resistance value could be used for all of the various contacts.

The rest of the circuit consists of approximations for the various sources and measurement devices. The AC sources in the model represent the output of a modulation-capable signal source (HP-8648D) through a high-pass filter (Minicircuits ZFHP-0R23-S+). The high-pass filter was included experimentally in an attempt to prevent any leakage from the modulation signal source at the modulation frequency. Initial experimentation and simulations (see Chapter 4) showed that even a small amount of leakage could have a significant impact on the small output currents measured. There-

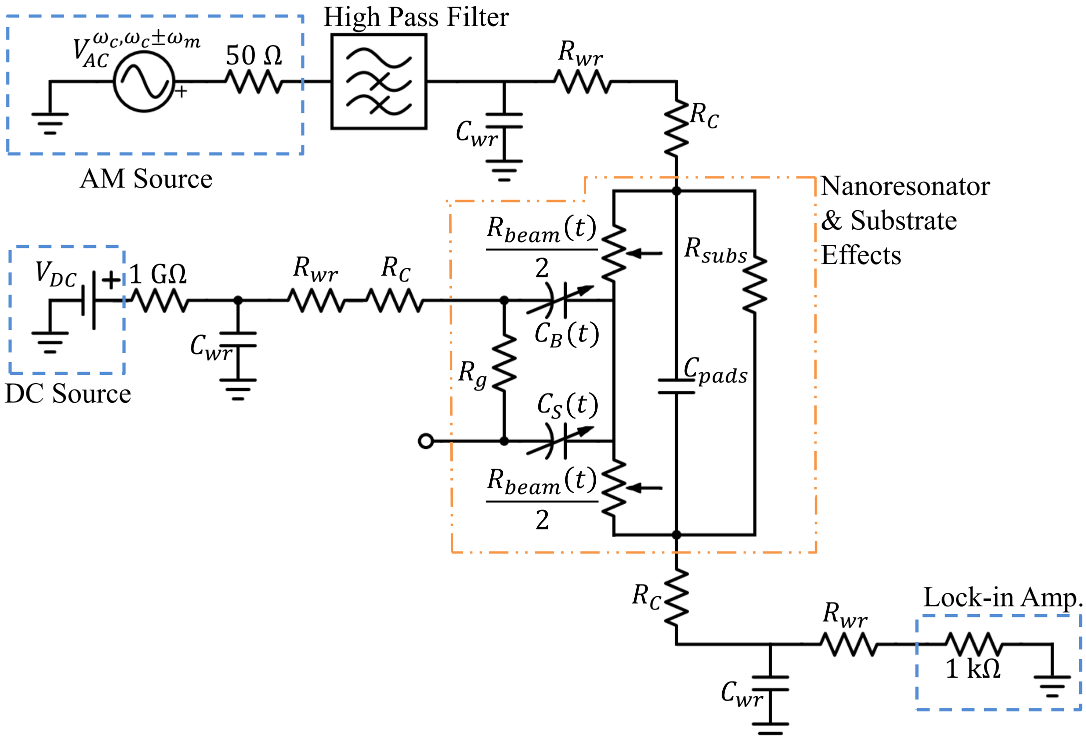

Figure 3.2. The final circuit schematic of the excitation system, device representation, parasitics and measurement system. The side gate is left floating in order to simplify experimentation.

fore, instead of capturing the full characteristics of the high-pass filter, the system was modeled as having an ideal, amplitude-modulated signal with a constant-amplitude leakage voltage, V_{leak}, at the modulation frequency. The lock-in amplifier (SRS-830) is modeled as a 1 kΩ resistor to ground, as suggested in the device documentation. While the probe station (Cascade Microtec PLV-50) has triaxial cable outputs, the lab equipment was uniformly equipped with biaxial junctions. Bufferless adapters were used and the parasitic prevention of the triaxial cables was lost. Therefore, the wires of the system were all considered as a capacitance to ground, C_{wr}, followed by a resistance, R_{wr}. The specific capacitance of the cables was both obtained from the supplier and measured in the lab as verification. The resistance of the wires was also measured and an average resistance was used for each implementation in the model. The 1 GΩ resistor following the gate source was used to prevent an excessive current flow through the device in the case of beam pull-in and is not part of a sub-system model.

3.2 Mixing Methodology for Response Detection

As electrical signals begin to enter the megaHertz range of frequencies and higher, the effects of system parasitics become more critical to consider. Slight leakage capacitances in a wire or between probes can cause a significant effect [39]. In order to overcome this, a common practice in the MEMS/NEMS field is to exploit the non-linearities of the system to excite it at resonance while measuring at an easily-tested frequency [8, 9, 33, 36, 39, 41, 43, 45, 65]. One such approach was implemented for this work. By applying an amplitude-modulated signal to the drain of the device, while applying a DC bias to the back gate, the forcing voltage,

$$V_{gap} = V_{dc} + V_{ac}\sin(\omega_c t) + \frac{mV_{ac}}{2}\sin[(\omega_c+\omega_m)t] + \frac{mV_{ac}}{2}\sin[(\omega_c-\omega_m)t], \qquad (3.1)$$

is obtained, where m is the ratio of the modulated signal's amplitude to the carrier amplitude, V_{ac}. The electrostatic forcing, and thus the vibration of the beam, is dependent upon the square of this voltage, leading to a beam vibration related to a DC component as well as ω_c, $\omega_c \pm \omega_m$, $2\omega_c$, $2\omega_c \pm \omega_m$, $2\omega_c \pm 2\omega_m$, ω_m, and $2\omega_m$. Since this produces a frequency component at the modulation frequency, ω_m, the output of the system will have a component that is created by the beam's vibration, which can be measured to obtain an approximate frequency response of the system. By sweeping the carrier frequency, ω_c, and measuring the output amplitude at the modulation frequency, an output can be obtained that gives an accurate image of the beam's behavior while avoiding many of the parasitics that present technical challenges to experimentation near the typical resonance frequencies of these devices.

While the mixing approach has its benefits, it is not without drawbacks. Because the percentage of the forcing that occurs at the modulation frequency is small, the final currents measured there are also small. For the majority of devices, this means attempting to measure picoAmperes of current at the system output. This is one of the primary motivations for the use of lock-in amplifiers to take measurements for these systems. Because a lock-in amplifier can measure the amplitude and phase of a single-frequency component with little noise, they are well suited for these mixing method measurements. The measurement of the modulation frequency also results in the loss of a large portion of information about the system. While the data will give an accurate representation of the beam's behavior, it is inherently missing the full frequency response of the system, and little is known about how the full electrical system will react to a single, higher frequency input in a true application of the system. This is problematic, since it is unlikely that a modulated input would be used with these devices in a practical application. From a mechanical standpoint it is also difficult to relate the system's output to a specific eigenmode of the beam [35]. Refer to Chapter 5 for a more in-depth review of the benefits and issues of measuring a down-mixed signal.

3.3 Obtained Response

Data was collected for multiple beams, varying in length and width but with consistent heights (110 nm). All of the beams were etched into the same wafer with the same orientation, so piezoresistive and material properties were identical for each beam. Figure 3.3 reflects a prototypical measurement response. The presented frequency response is that of the amplitude and phase of the modulation frequency component at the source pad. All testing was completed using $\omega_m = 1$ kHz. Both the amplitude and phase exhibit hysteresis, evidence of a region of bistability that occurs around the resonance. As expected, the responses generally match the shape of a hardening Duffing response. It is also seen that due to the nonlinearities of the system, the DC bias on the back gate leads to tuning of both the amplitude and frequency of the resonance curve. This effect will be further explored in Section 4.3.2.

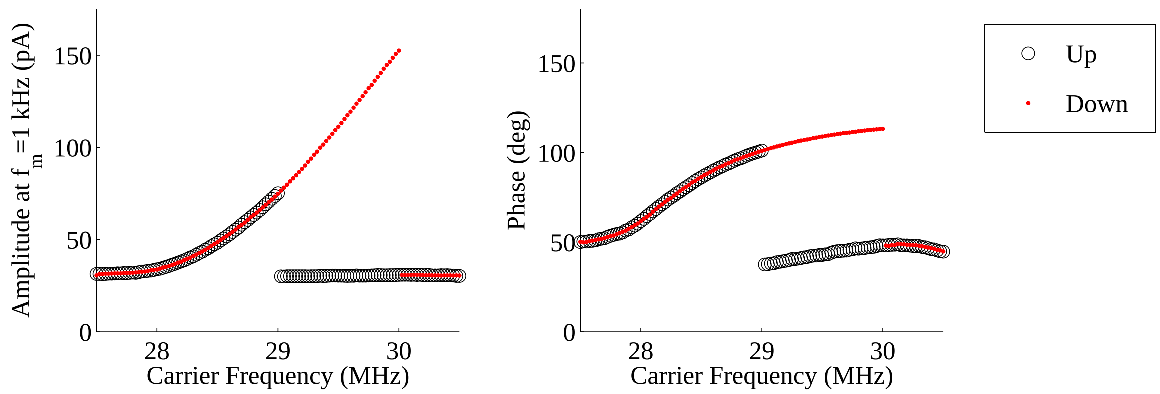

Figure 3.3. The amplitude (left) and phase (right) response of the modulation frequency, $f_m = 1$ kHz, for a characteristic experimental measurement. Both the increasing and decreasing frequency sweeps are included to visualize the hysteretic nature of the system. The nanobeam used had a length of $L = 4$ μm and width of $w = 180$ nm. The excitation levels were $V_{dc} = 6$ V and $V_{ac} = 40$ mV$_{rms}$.

Because devices from this same wafer had been previously examined in [14], it was possible to compare the current responses to those obtained previously. The primary resonances are very similar. For comparable forcing voltages, the bandwidth of the response is approximately the same. While the amplitude of the response varies, this can easily be attributed to geometric differences in the beam. The previous data collected in [14] identifies two different resonances, one for each gate, even though only one gate had a nonzero potential. This difference can be traced to the practice of grounding the side gate in [14]. When the second gate is grounded instead of left floating (as is the case in this work), the extra gate maintains a fixed potential, leading to a second forcing voltage actuating the beam. Therefore it is not incorrect to view only a single peak in the results presented here, while two responses were observed in the prior work.

CHAPTER 4. SYSTEM-LEVEL SIMULATION

In order to compare the results produced by the modeled system and those found experimentally, it was prudent to compile and implement the various aspects of the presented model to form a numerical simulation of the nanosystem's behavior that could be easily combined in a circuit simulator with standard circuit components and other compact models. Once developed, the functionality of the simulation was verified by independently solving the base system of equations using numerical methods. The overall performance of the model was then confirmed through comparisons with the experimental results in Chapter 3. By allowing for the rapid generation of circuit designs, the simulation enables the testing of situations that could not be easily developed experimentally. This allows for the investigation of both device-level and system-level behaviors that could only be inferred with great difficulty from laboratory data.

4.1 Simulation Description

Using Verilog-A, the differential and algebraic equations (see Chapter 2) describing the system were coded to form two separate, but dependent, numerical simulations, which when used together effectively simulate the beam's electromechanical behavior. One simulation captured the electrostatic effects and beam motion, by accepting the beam-gate voltage as an input and determining the beam displacement and current flow as outputs. The other simulation accepted the voltage drop across the beam and the beam displacement as inputs to determine the current through the beam when accounting for piezoresistive effects. These simulations represented the variable capacitors and resistors in Figure 2.3, respectively.

The Verilog-A components could be combined with any other standard or custom circuit components and simulated, using the Spectre (a derivative of the SPICE simulator) harmonic balance solver to determine the steady-state outputs of the system. Using the circuit presented in Figure 3.2 and plotting the outputs from the harmonic balance solver, it was possible to generate plots directly reporting the same information acquired experimentally. These plots depict changes in the amplitude and phase of the signal at the modulation frequency as the carrier frequency is varied. The simulation was also capable of producing transient waveforms and other results, which can provide a dense amount of information about the system, but the harmonic balance results provided the most direct comparisons to experimental data.

The nominal parameters used in the simulation were selected to correspond to the systems tested experimentally. The beam had a height, h, of 110 nm, and the back and side gates have nominal gap sizes of $g = 144$ nm and $g_s = 200$ nm, respectively. The beam was considered to have no residual stresses present after fabrication. $\rho = 2330$ kg/m^3 is the density of silicon. The beam was approximated to have a value of $c \approx 0.6E{-}6$ kg/(m·s), the specific damping constant of the system as described in Section 2.1. As discussed in Section 2.2.3, the crystal orientation of the beam changes several of the effective material properties of silicon. The simulation was setup to correspond to a crystal in the $< 111 >$ orientation, consistent with the beams tested experimentally. This resulted in $E = 187.5$ GPa and $\nu = 0.17$ [66], where ν is Poisson's ratio. While the length and width of the beam were two of the most common parameters varied, the most common combinations were $L = 6.3$ μm, $w = 120$ nm and $L = 4$ μm, $w = 180$ nm, which correspond to two of the experimentally analyzed beams. The amplitude modulation of the input signal was kept at a constant modulation index – the parameter defining the height of the side bands in the modulated signal – $m = 0.5$, and modulation frequency, $f_m = 1$ kHz. V_{ac}, V_{dc} and f_c – the amplitude of the carrier signal, the DC bias, and the carrier frequency, respectively – were used as the inputs to the system. Several basic electrical parameters, such as R_{wr}, R_c, R_g, and C_{wr} were measured from the experimental setup or obtained by other approximations, as discussed in Section 3.1. It should be noted that many of these values, and those not listed here, but included in Table 4.1, have some measure of uncertainty. For example, there are fabrication tolerances associated with the physical dimensions of the device and the exact doping level. Other parameters, such as contact resistance, are highly uncertain (see Section 3.1).

4.2 Solution Algorithms

Regardless of the algorithm used, Spectre utilizes general tolerance variables to define the accuracy required from the solution. The *reltol*, *iabstol*, and *vabstol* variables set the relative tolerance of both the current and voltage values, and the absolute tolerance of the currents and voltages, respectively. To reach convergence, the change in the current must meet

$$\Delta i < reltol * (\text{largest current into the node}) + iabstol. \tag{4.1}$$

Similarly, the voltage must satisfy

$$\Delta V < reltol * max(\text{initial voltage, final voltage}) + vabstol. \tag{4.2}$$

When these conditions are met at every node, the step is considered to be converged. Note that the size of the signals determines whether the absolute or relative tolerance is the dominant constraint. For small signals, the absolute tolerance will dominate, while the relative tolerance of a large signal is the limiting parameter. For both the time domain and harmonic balance approaches, all tolerance values were set to $1E{-}8$ to provide an accurate solution even with the small amplitudes inherent with nanoscale systems.

4.2.1 Time Domain Solution

The simulation provides the ability to numerically integrate the full circuit and beam system to determine its time domain response. There is the potential to provide detailed information about the transient behavior of the forcing voltage, system

Table 4.1. Nominal Parameter Values.

Parameter	Value
E	187.5 GPa
ρ	2330 kg/m^3
h	110 nm
g	144 nm
c	$0.6E{-6}$ kg/(m·s)
S_r	0 Pa
R_{lock}	1000 Ω
R_{wr}	4 Ω
R_c	2 Ω
R_{subs}	10 TΩ
R_g	263 kΩ
R_r	1 GΩ
R_{beam}	51.2 kΩ
C_{wr}	0.6 nF
C_{pads}	1.45 fF
C_s	0.029 fF
π_L	1.403 1/GPa

currents, as well as the beam displacement and velocity. Spectre's transient analysis utilizes three solving algorithms: backwards-Euler, trapezoidal, and Gears second-order backwards-difference, each of which can also be used in combination to achieve various balances of accuracy and speed. For the tests presented here, the Gear method with conservative error tolerances was utilized to get a solution without ringing and false stability. While this method can provide a great insight into the system's behavior, it is typically slow. This is especially true with regard to a modulated input case, because of the extended periods of time required to capture low-frequency components like the modulation frequency.

4.2.2 Harmonic Balance Solution

The harmonic balance solver used a two-step approach to compute the steady-state response of the system at specific frequency components. It first finds a DC operating point for the circuit and then uses Newton methods to converge upon steady-state values for the full system. For the typical simulations presented here, the harmonic balance approach required consideration of at least 8 harmonics for both the carrier and modulation frequencies to produce a solution which did not change upon the addition of further harmonics. In some cases, 14 harmonics were required for a proper convergence. Depending on the amplitude of the response, either transient-aided solving or source stepping homotopy methods were implemented to achieve an initial operating point that would generate a converged steady-state output. The transient aided homotopy develops an initial guess for the harmonic balance analysis using a transient analysis, making it a more robust approach and useful in cases where the amplitude of the system states was small and convergence was difficult. The source-stepping homotopy approach gradually varies the source level in order to reach a converged solution, and uses that as an initial guess. Therefore it can be useful for strongly nonlinear systems. Generally, the transient-aided approach was more reliable, but significantly slower ($\sim$15 minutes/2 MHz sweep increasing through resonance), than source-stepping ($\sim$5 minutes/2 MHz sweep increasing through resonance).

It was generally noted that if a simulation failed to converge, the failure occurred at the discontinuity associated with a bifurcation. Larger amplitude responses tended to have fewer issues, presumably due to the fact that smaller amplitudes result in a smaller tolerance zone where convergence can be achieved. As a corollary to this, increasing frequency sweeps tended to solve more reliably than decreasing sweeps, since the hardening response results in the up-sweep exhibiting a larger amplitude. Convergence is more easily obtained when the system's bifurcation drives the amplitude toward zero, as opposed to an indeterminate value as is the case for the down sweep. Thus, it is common to require an extended transient-aided solving period when computing a decreasing frequency sweep.

4.3 Performance Validation

In order to confirm that convergence was properly achieved, while simultaneously providing validation of the model, the simulation results were compared to numerical integrations of the base model as well as to experimental results.

4.3.1 Simulation Setup

In order to confirm that the simulation was running properly and that all tolerance values had been appropriately set, a simulation of the base circuit presented in Figure 2.3 was compared against a numerical integration of Equations (2.35)-(2.37), performed in Matlab. The numerical integration was performed using Matlab's ode15s routine. An implicit, variable-order solver, ode15s is designed for stiff differential equations and differential-algebraic equations like the ones under consideration here [67]. The numerical integration was iteratively solved for all of the frequencies, utilizing the steady-state conditions of one solution as the initial conditions for the next input frequency. This continuation method allowed for a direct comparison of the frequency responses obtained from Spectre. This method proved advantageous to a direct comparison of the transient data simply as a reduction in the sheer amount of information present. Viewing the frequency response also presents a better picture of the simulation's ability to capture the desired information about the system.

When the time domain results at a single frequency are compared there are discrepancies in the transients between Spectre and Matlab, but the steady-state responses match. The frequency responses showed that the simulation accurately represents the derived equations. Furthermore, Spectre could achieve the same frequency response faster than what could be achieved using Matlab. Additionally, while it was possible, with changes in the tolerance settings, to cause the Matlab numerical integration to bifurcate earlier along the backbone, this was attributed to a lack of accuracy in the continuation method due to a larger frequency step than that used in Spectre. The added accuracy that can be obtained from the circuit simulation due to its speed is a major advantage encouraging its use.

4.3.2 Modeled Response

By developing a simulation that captures all of the elements present in Figure 3.2 and by analyzing the results of a harmonic balance sweep at the modulation frequency, it was possible to compare the proposed model for the overall system with the experimental data. Order-of-magnitude approximations were used for the variables with large degrees of uncertainty, such as the specific damping coefficient. Figure 4.1 shows the response for both the increasing and decreasing sweeps of the carrier frequency without any detailed parameter refinement. Away from resonance there is a small, flat background current and the phase approaches a constant value. Near resonance the response becomes bistable and exhibits hysteresis, symbolic of bifurcations occurring in the nonlinear system. The resonant frequency of the system is defined here as the frequency associated with the largest peak current. While discrepancies exist, it is probable that these differences could be attributed to the intrinsic variability of the nominal system parameters. The most notable discrepancy is that the resonant frequency predicted by the simulation is much larger than what is seen experimentally.

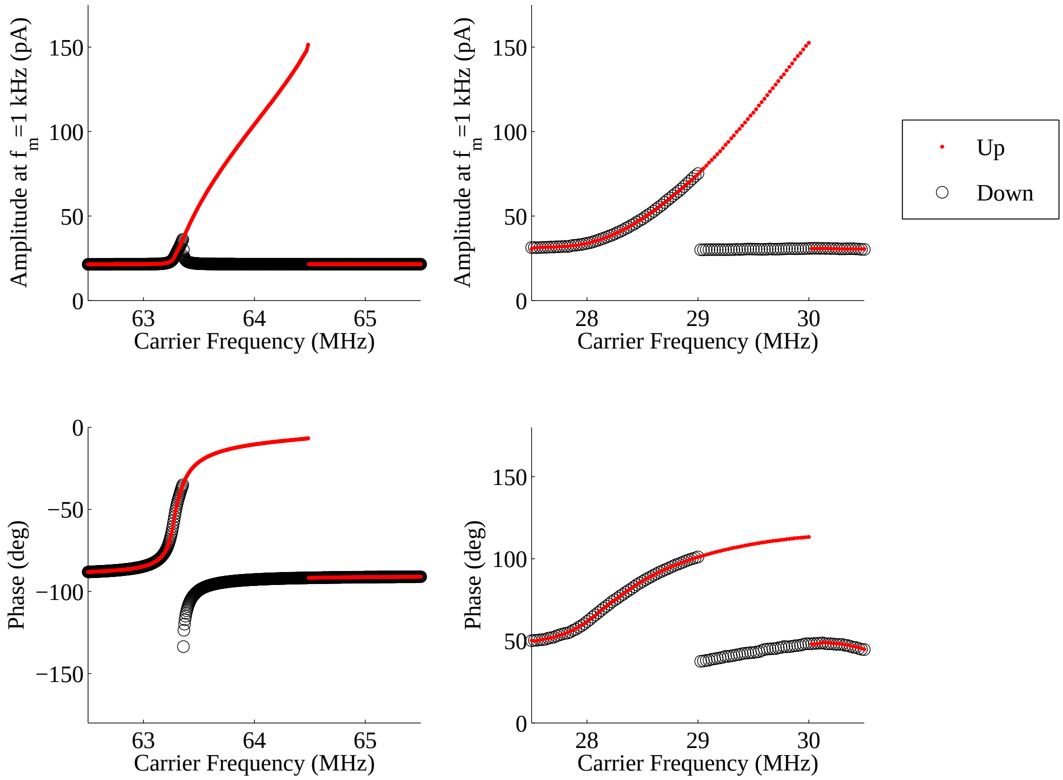

Figure 4.1. A comparison of the simulated (left) and experimental (right) results for both response amplitude (top) and phase (bottom). The results are collected at the modulation frequency of the input, here 1 kHz, as the carrier frequency is either increased or decreased around resonance. Note that, $V_{dc} = 6$ V, $V_{ac} = 40$ mV$_{rms}$, $L = 4$ μm, and $w = 180$ nm.

When a scanning electron micrograph was taken of the beam location after testing was completed, Figure 4.2, it was found that the trench, including the visible undercutting at the edges, measured approximately 4 μm, the length used for the simulation in Figure 4.1. It was noted that the pad-to-pad distance was roughly between 5.7 and 6 μm. If the simulation is instead run for a beam of length $L = 5.9$ μm, the frequency and bandwidth of the hysteretic region more closely matches what is seen experimentally, as seen in Figure 4.3. This would suggest that the entire length of the beam was released from the substrate during the fabrication process, rather than just across the trench.

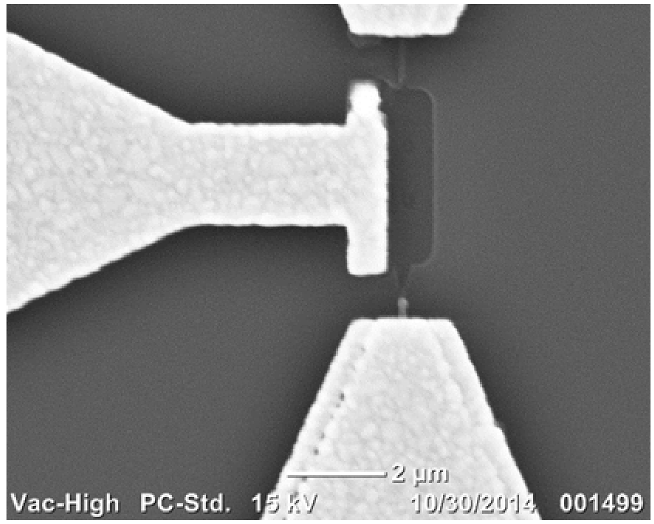

Figure 4.2. An SEM of the beam location for the experimentally tested device. The beam was destroyed following testing, but the trench size gives an estimate of the suspended length of the beam. The trench length, including visible undercutting, is approximately 4 μm. The pad-to-pad length of the beam is roughly 5.7 to 6 μm. Photo Credit: Hossein Pajouhi.

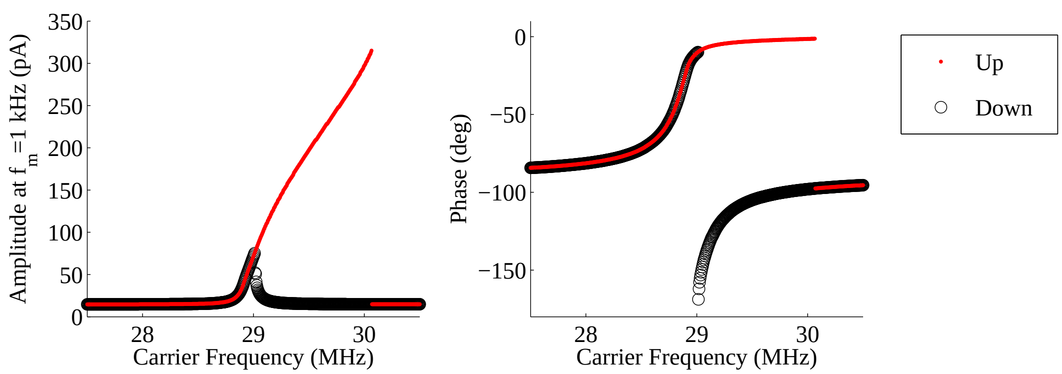

Figure 4.3. The response amplitude (left) and phase (right) collected at the modulation frequency of the input, here 1 kHz, as the carrier frequency is either increased or decreased around resonance. Note, $V_{dc} = 6$ V, $V_{ac} = 40$ mV$_{rms}$, $L = 5.9$ μm, and $w = 180$ nm.

The discrepancies in Figure 4.1 can also be diminished by making variations to the residual stress and damping, which are both very difficult to measure and predict, one can shift the response to a similar frequency and amplitude, as seen in Figure

4.4. In this case, the differences in bandwidth and off-resonant current could be explained through variations in a combination of other parameters. For example, the leakage voltage at the modulation frequency plays a large role in determining the nonzero off-resonant response as well as the shape of the phase response. Similarly, the amplitude of the response could be shown to be highly dependent upon the effective piezoresistive coefficient, which was shown in [46] to be dependent on diameter for a silicon nanowire, but has not been fully characterized for nanobeams. Any size correction was therefore neglected here and could result in the observed errors. It was anticipated that, given the proper parameter set, the model would accurately provide the down-mixed response near the first-mode beam resonance.

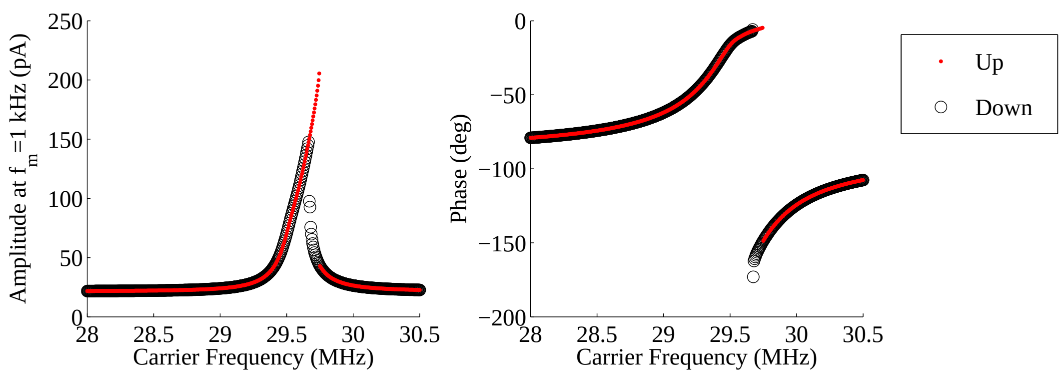

Figure 4.4. The response amplitude (left) and phase (right) collected at the modulation frequency of the input, here 1 kHz, as the carrier frequency is either increased or decreased around resonance. Note, $V_{dc} = 6$ V, $V_{ac} = 40$ mV$_{rms}$, $L = 4$ μm, and $w = 180$ nm. The compressive residual force, S_r, is -375 MPa and $c = 6E{-}6$ kg/(m·s).

Further verification of the model was obtained by analyzing the tuning behavior of the resonant response for varying DC bias levels. Figure 4.5 shows the experimental and simulated impact of the gate bias, V_{dc}, on both the peak amplitude and resonant frequency for a beam with $L = 6.3$ μm, $w = 120$ nm. The responses have been normalized around their values at 2 V in order to facilitate a qualitative comparison in the face of unrefined parameter estimates for the simulation. A quadratic increase in amplitude and decrease in frequency is present in both the simulation and experimentation. The responses are similar, even when only rough estimates of the parameters are used. While the simulation and experimental data could be used to complete a parametric study and improve the accuracy of the parameter estimates, the qualitative match between the simulation and experiment was sufficient to suggest that the model was adequately capturing the major dynamics of the system. A complete parameter identification for the system would prove to be exceedingly difficult using down-mixed methods. This difficulty arises from the various frequency regimes where the parameters affect the system. In general, several parameters have exceedingly minor effects at the low frequencies observed in the mixing methodology. This prohibits proper identification of certain parameters when a down-mixing scheme is used, since wide variations in the parameters can have only small effects on the observed response. Reliance on the simulation instead of a closed-form analytical solution also makes parameter identification exceedingly slow. Thus, the qualitative fit was considered satisfactory to provide observations on the nature of the device response.

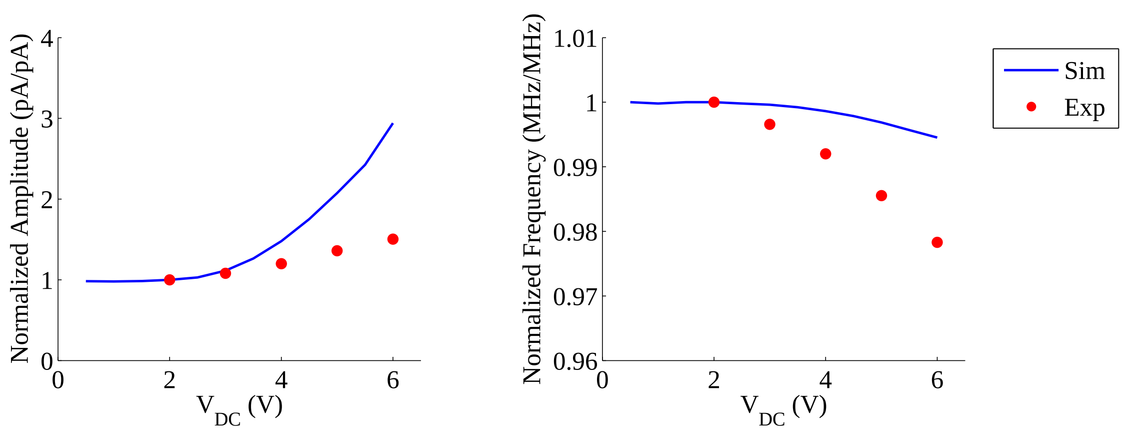

Figure 4.5. The effects of increasing the DC back-gate bias for a constant amplitude-modulated signal across the beam, while $V_{ac} = 15$ mV$_{rms}$. The peak amplitude (left) and resonance frequency (right) responses are normalized around their 2 V levels to facilitate qualitative comparisons in response nature. $L = 6.3$ μm, $w = 120$ nm.

4.4 Practicality of Use

Due to the interconnected nature of an electrical circuit, the change of a single component can result in a large computational overhead to recompute the response if the system is solved by re-deriving all of the relevant circuit equations. Numerically solving the response of the circuit proves to be an excellent alternative for the rapid design and prototyping of circuits. By bringing the complicated nonlinear dynamics of the nanoresonator system into this environment, the ability to investigate the potential of the device increases drastically. The ability to predict how the device would react in complex circumstances or studying how changes in the beam and material parameters affect the output, becomes straightforward. Furthermore, the simulation provides the ability to determine what the device would do in a commercial environment. With the ability to measure results, such as a high-frequency response, it is possible to predict the system's response in a way that could not be determined in the lab. An investigation into the fundamental understanding of the system's dependencies, as revealed by the simulation, will be presented in Chapter 5. Chapter 6 focuses on presenting the power of the simulation to demonstrate what the nanobeam system can achieve when placed in a variety of circuits.

CHAPTER 5. MODEL ANALYSIS

5.1 Frequency Mixing Effects

Section 3.2 describes the mixing approach used to experimentally characterize the nanoresonator's response. While an amplitude-modulated input is representative of an input with multiple frequency components, the proposed applications for many NEMS devices do not require, or even desire, mixing (with a few exceptions, i.e. [36]). Therefore, the simulation was used to predict the system's response to a single-frequency input, measuring the amplitude and phase of the output current at the same frequency as the excitation. This was done with the same test circuit used in the modulation testing (Figure 3.2), with different input/output signal configurations. Note that no power correction was made to adapt for the loss of the side bands when adjusting from the amplitude-modulated signal to the single-frequency signal.

Figure 5.1 presents the responses from the simulation for sweeps of increasing frequency for both the modulated input, measured at the modulation frequency, as well as a single-frequency input, measured at the excitation frequency. A qualitative change in both the amplitude and phase response is immediately apparent, especially as the resonant peak becomes an antiresonance. Equally importantly is that the location of the resonant peak changes between the cases. For the modulation case, the resonant frequency is around 25.75 MHz. However, when only the single input frequency is used, the resonant frequency is varying around 26.75 MHz. The difference in behavior exposes an issue with the methodologies common in testing NEMS to date. If the modulation case does not accurately predict the resonant frequency or tuning behavior for cases similar to possible final applications, such as a single-frequency excitation, then the devices cannot be properly designed for those final-use cases based upon current experimental methods. Figure 5.2 exposes a similar issue for variations

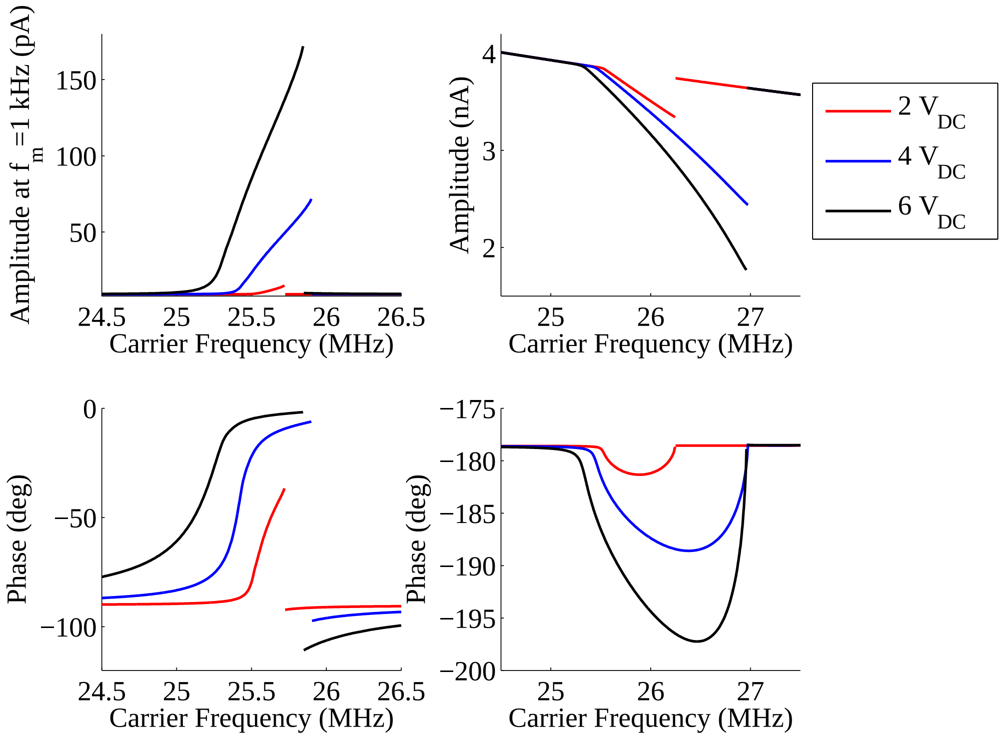

Figure 5.1. The amplitude (top) and phase (bottom) responses for an amplitude-modulated signal measured at the down-mixed modulation frequency (left), as well as for a single-frequency excitation, measured at that frequency (right), for various DC bias amplitudes. Note the change in the shape of the responses, as well as the changing resonance frequencies and tuning behavior. Also note, $V_{ac} = 40$ mV$_{rms}$, $L = 6.3$ μm, and $w = 120$ nm.

in the AC voltage of the carrier, while maintaining a constant DC bias. Even if a single-frequency input does not fully represent a final-use case, the presence of a resonance shift corresponding to an input variation implies that accurate predictions of final behavior cannot be made using down-mixed testing. Reference [8] exhibits a similar shift in system resonance frequency with a change from frequency-modulated testing to amplitude-modulated testing.

As an aside, it is interesting to note that the tuning behavior in Figure 5.1 does not match the curve in Figure 4.5. This implies that the tuning curve varies with the AC amplitude applied, which is a reasonable conclusion considering the nonlinear nature of the system. Both the AC and DC variations show differences in the amount of tuning observed when comparing a modulated case to a single-frequency case. This only serves to further complicate any device implementation based upon down-mixed data. The relation between the excitation power and the frequency response is further explored in Section 5.2.

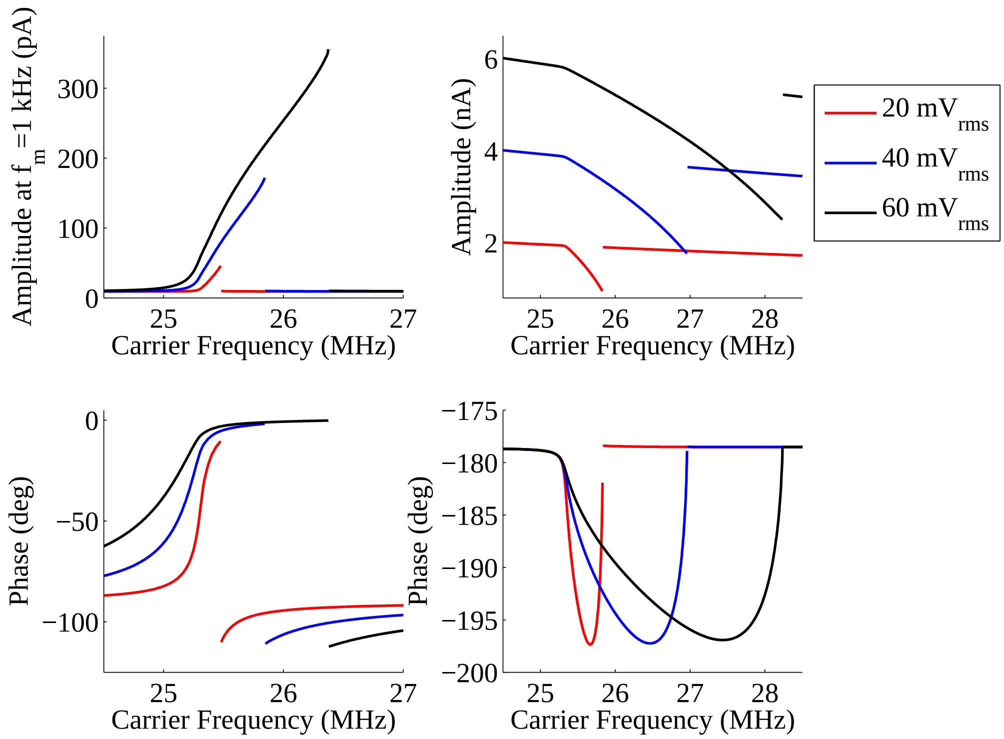

Figure 5.2. The amplitude (top) and phase (bottom) responses for an amplitude-modulated signal measured at the down-mixed modulation frequency (left), as well as for a single-frequency excitation, measured at that frequency (right), for various AC signal amplitudes. Note the change in the shape of the responses, as well as the changing resonance frequencies as V_{ac} changes. Also note, $V_{dc} = 6$ V, $L = 6.3$ μm, and $w = 120$ nm.

The development of NEMS for final usage at any level depends on understanding how the associated device will respond to stimuli when in use. Because the classical mixing methods used for testing fail to capture all of the response behavior in the regime where devices, such as the nanoresonator presented here, will be operating, the responses and properties from the modulated data, especially the system resonance frequency, cannot be used to predict the device's behavior in a final application. For example, if the device here were to be used in a tunable filter design and built to operate at a frequency and DC bias determined from the down-mixed data, then the results presented here suggest that there is no guarantee the final passband of the filter would be where it was designed to be. In fact, the variation between the modulation and single-frequency cases suggests that the filter would experience changes in its passband location as the number of frequency components it receives varies, essentially negating its usefulness as a filter. This is made evident by the shifts in the system resonance frequency as the amplitude of the applied AC current is increased. Any practical application of a filter is likely to receive a signal with a changing number of frequency components and amplitudes, and both changes have been shown to produce variations in the system resonance frequency. Either a test procedure must be developed to enable accurate testing of NEMS devices in final-use scenarios, or testing is needed to determine if there is a region, perhaps under a larger DC bias, where the changes in the AC signal have less of an impact upon the nature of the device response. If such a region were to exist, then the down-mixed results may be a more appropriate predictor of device behavior.

5.2 Natural Frequency Estimation

The defining feature of any resonant system is its resonance frequency. Therefore, it is important to be able to design systems to operate at a specific frequency. The previous section indicates a need to better understand the tuning behavior of these systems in order to make that possible. Towards this end, it is advantageous to develop an estimation of the linear natural frequency for the system. While the nonlinearities in the system clearly shift the resonant frequency away from the natural frequency, especially when the interactions between the beam voltage and displacement are considered, the natural frequency of the undamped, linear system provides a decent approximation of the peak amplitude's location.

In a linear sense, the natural frequency can be defined as

$$\omega_n = \sqrt{\frac{K_{eff}}{M_{eff}}}, \tag{5.1}$$

where K_{eff} is the effective stiffness of the beam and M_{eff} is the effective mass. For the nondimensional definition of the beam equation, Equation (2.36), this is equivalent to

$$\hat{\omega}_n = \sqrt{-\alpha_{10} - \alpha_{11}\left[\hat{V}_b(\hat{t}) - y_3(\hat{t})\right]^2}. \tag{5.2}$$

The residual stress left in the beam from fabrication, $\hat{s}$, is part of α_{10}, and contributes to the nominal resonant frequency, such that an increase in the compression of the beam leads to a decrease in the nominal frequency. The dimensional value of the nominal natural frequency, defined for no electrostatic forcing, will be

$$\omega_n = \sqrt{-\alpha_{10}}\omega_0\sqrt{\frac{Eh^2}{12\rho L^4}}, \tag{5.3}$$

which will be lower than the frequency that would be predicted by the standard linear beam model because of the nonlinearities within the system.

To study the electrostatic tuning, it is desirable to substitute Equation (2.9) into Equation (5.2). Since the desired estimate of the natural frequency does not vary with time, the time-varying voltages can be replaced by their RMS equivalents to relate the frequency to the estimation of the forcing power, $\hat{V}_{gap,rms}$. Differentiating the resulting equation provides the tuning sensitivity,

$$\frac{\partial\hat{\omega}_n}{\partial\hat{V}_{gap,rms}} = \frac{-\alpha_{11}\hat{V}_{gap,rms}}{\sqrt{-\alpha_{10} - \alpha_{11}\hat{V}^2_{gap,rms}}}. \tag{5.4}$$

Equation (5.4) enables a relation between the beam design and the natural frequency of the system.

An increase in the forcing voltage will lead to an increase or decrease in the natural frequency based upon the sign of α_{11}, which is driven by the aspect ratio of the beam, $\hat{L}$. For α_{11} greater than zero, the natural frequency decreases, coherent with the standard electrostatic softening effect. However, based upon the definition of α_{11} (Table 2.3), for values of $\hat{L} < 1.3655$, α_{11} will be negative and result in an electrostatic hardening effect. To achieve this, the system must have a beam that is nearly the same size as the nominal gap. Based upon fabrication restrictions for the possible gap sizes, this requires a short beam. Correspondingly, the natural frequency of that arrangement is likely to be large, since the beam height required to compensate for such a short length is not feasible. This limits the realm of frequencies where an increasing tuning can be achieved.

The nonlinear nature of the system will result in a resonant frequency and tuning that is only approximated by what is predicted for the natural frequency in Equation (5.2). Figure 5.3 shows this discrepancy. While the resonant frequency of the increasing frequency sweeps does not follow the predicted behavior, the peaks of the decreasing frequency sweeps are very close to what is predicted by the natural frequency. Note also that a small change in the AC voltage produces a large change in up-sweep response, suggesting that the RMS approximation is poor and the presence of harmonic content has a large effect on the nonlinear portions of the system that lead to this response.

The dependence of $\hat{V}_{b,rms}$ and $y_{3,rms}$ upon the circuitry encompassing the nanobeam implies that the design of the beam should be dependant upon the circuitry involved. Alternatively, it is possible to design the beam for a frequency slightly higher than desired and electrostatically shift the resonant frequency to its desired location through the use of the DC bias. The advantage of this method is that it is immune to nearly all fabrication and design tolerances, as long as the nominal resonance frequency does not require so large a forcing power that the beam is pulled-in during tuning. In all, there is some explanation of the tuning observed in Section 5.1, since the change in the signal power due to the presence or absence of the amplitude-modulated side bands could explain some of the tuning. However, this does not alleviate the concerns

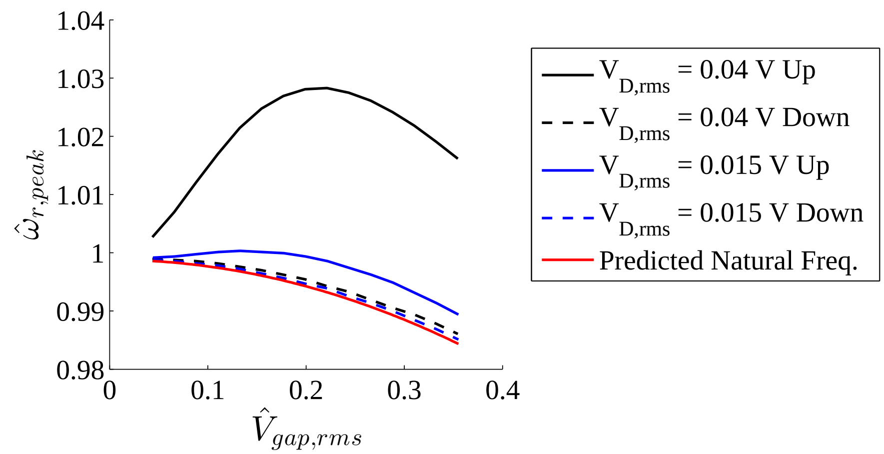

Figure 5.3. Electrostatic tuning of the beam's simulated resonant frequency as compared to the predicted natural frequency. The presence of the nonlinearities, as well as the interactions between the beam displacement and voltage, result in large discrepancies between the resonant and natural frequency responses in the increasing frequency sweeps. The tuning of the peak amplitude in the down-sweep responses matches the linear natural frequency prediction well.

that Section 5.1 raises about the implications of this phenomena for the practical use of these devices as filters.

5.3 Design for Softening

The frequency responses shown thus far have all exhibited hardening characteristics, where the nonlinearities of the system have increased the frequency at which the peak amplitude is observed above the predicted natural frequency. In practice, the ability to design the system to instead exhibit a softening response, where the peak frequency is below the linear natural frequency, could be beneficial. When combined with the ability to tune the frequency of the response, this creates a very flexible and powerful system. For a standard Duffing resonator, the presence of a hardening or softening frequency response can be predicted using the sign of the cubic stiffness term. For a system such as the one presented here, with a combination of both cubic and quadratic nonlinearities, the sign of a linear combination of both terms indicates the direction of the frequency backbone. Under the same approximation of RMS voltage used in Section 5.2, this linear combination, represented by α_{nl}, is

$$\alpha_{nl} = -p_2 \alpha_2 \hat{V}^2_{gap,rms} - p_3 \left(\alpha_{30} + \alpha_{31} \hat{V}^2_{gap,rms} \right), \tag{5.5}$$

where p_2 and p_3 are proportionality constants defined by the system parameters and interactions. They could be analytically approximated using perturbation methods, or experimentally approximated by using regression techniques. It is the sign of α_{nl} that will indicate the system's preference for a hardening or softening response.

Equation (5.5) demonstrates the dependence of the response shape to the electrostatic forcing. With this relation, it is possible to develop a single beam which could be tuned between a hardening and softening response using the electrical loading of the device. Under the substitution,

$$p_2 = p \times p_3, \tag{5.6}$$

the voltage required to achieve a softening response becomes

$$\hat{V}_{gap,rms} > \sqrt{\frac{-\alpha_{30}}{p\alpha_2 + \alpha_{31}}}. \tag{5.7}$$

The voltage criterion is then not only dependant upon the unknown proportionality between the quadratic and cubic nonlinearities, but is also heavily dependant on the geometry and mode shape of the beam through α_2, α_{30}, and α_{31}. Even if the system is such that p is small, if α_2 is sufficiently larger than α_{31} then the frequency backbone will still be dominantly influenced by the quadratic term. For an initially straight beam, such as the one used for the generation of the terms in Tables 2.3 and 2.4, the cubic terms will dominate the response backbone, since the equation of motion for the beam, Equation (2.1), features no quadratic terms. Any quadratic effects arise solely from the electrostatic forcing and are thereby naturally weaker than the cubic term, which has contributions from both the beam's mid-plane stretching and the electrostatic forcing. In this configuration, it proves very difficult to achieve a softening response. For the beam described by Tables 2.3, 2.4 and 4.1, with an assumed dominant cubic solution (approximated here by $p = 0$), the minimum nondimensional voltage to obtain a switching response is 1.9209, nearly twice the pull-in voltage.

In contrast, an initially arched beam is likely to exhibit a stronger quadratic geometric nonlinearity, which could drastically change the response shape. Practically speaking, it is reasonable to assume that the majority of fabricated beams will have some form of an arch as the support structure underneath them is etched away. Therefore, it is difficult to quantitatively specify the ability of the system to achieve a softening response for a system with an unknown amount of initial arch. However, in terms of aiding future designs, the criterion are clear that an initial curvature would be very beneficial in this effort.

CHAPTER 6. CASE STUDIES

The primary advantage of the simulation is its ability to rapidly iterate designs. Because of the ease with which it allows the combination of custom beam dynamics and standard circuit components, it is possible to determine the effect of a full circuit very quickly and with reasonable accuracy. To exploit this, several case studies were performed to better understand the dynamics of the system and to verify the practicality of the nanoresonator.

6.1 AC/DC Application Effects

Inspired by the differences in the modulation and single-frequency inputs observed in Section 5.1, a study was conducted to investigate the effects of various input configurations. Specifically, the differences between AC and DC applications on each node was investigated.

6.1.1 Simulation Setup and Results

Simulations were performed for six input cases, listed in Table 6.1. In each case, the nanobeam had a cross section of 120 nm wide by 110 nm tall, and was 6.3 μm long. All other parameters were congruent with those found in Table 4.1. The simulations used a single-frequency, harmonic input instead of a modulated input, and analyzed the component of the output current at the input frequency. For simulation purposes, it was assumed that the output node was connected to ground, and any floating node was left unspecified in Table 6.1. Spectre's harmonic balance solver was used to compute the frequency response with a transient-aided homotopy stop time of 10 ns and with the inclusion of 13 harmonics for the carrier frequency. The AC input was 40 mV$_{RMS}$, while the DC bias used was 6 V.

Table 6.1. Input Cases.

Case	Drain	Source	Gate
1	AC	OUT	DC
2	DC	OUT	AC
3	AC+DC		OUT
4	OUT		AC+DC
5	OUT	OUT	AC+DC
6	AC+DC	AC+DC	OUT

Figure 6.1 displays the frequency response of the output current for the various input cases. Of note is the fact that Cases 3 and 4 are identical, as are the responses for Cases 5 and 6. This proves the symmetry of the model because these loading conditions are simply opposites of each other across the beam-gate gap. Interestingly, each case provided a different peak frequency and response amplitude. These amplitudes and frequencies are recorded and sorted in Tables 6.2 and 6.3. Case 1 is the only response that features a significant off-resonant output current and features an anti-resonance instead of a resonance. Cases three through six exhibited a small off-resonance current, but not as small as that observed in Case 2.

Table 6.2. Response Resonance Frequencies.

Case	Frequency (MHz)
1	26.96
3 & 4	27.64
2	29.37
5 & 6	29.43

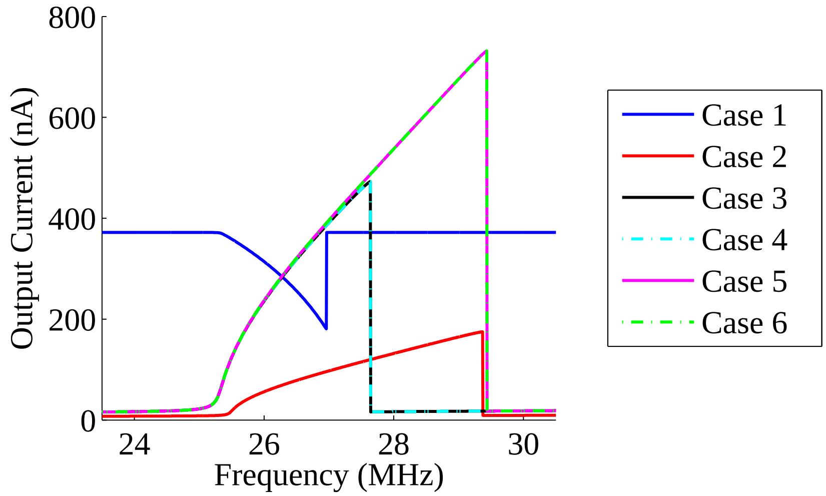

Figure 6.1. Output current magnitude for different circuit connections. Cases 3 and 4, as well as 5 and 6, are identical due to the symmetry of the system. The various cases result in changes in the response amplitude, frequency and shape. $V_{ac} = 40$ mV_{rms}, $V_{dc} = 6$ V, L = 6.3 μm, $w = 120$ nm.

Table 6.3. Resonant Amplitude Increase Above Background.

Case	Increase (nA)
1	-191.2
2	165.7
3 & 4	456.5
5 & 6	714.0

6.1.2 Explanation of Responses

In order to explain the discrepancies in peak frequency and the variations in amplitude between the different cases, the circuit was analyzed at both near- and off-resonant frequencies. In the off-resonance case, the beam has a negligible amount of motion allowing the piezorestive properties of the beam to be approximated as a static resistance, say R_0, and the beam-gate capacitance as a static capacitance, say C_B. In this case, the substrate resistance R_{subs} is much greater than the beam resistance, and can be approximated as an open connection. The resulting schematic for the off-resonant device can be found in Figure 6.2. In order to match the simulation, the output node is treated as the reference potential (i.e. ground). In Case 1, the

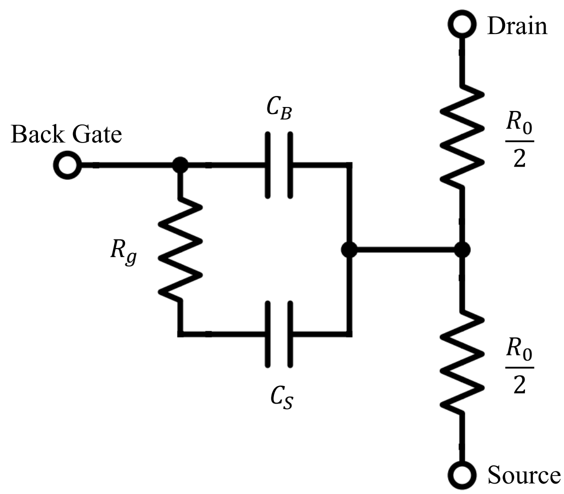

Figure 6.2. Circuit schematic for an off-resonant excitation, including leakage through the side gate.

AC signal on the nanobeam cannot jump the capacitive gap to the gate, since the gate is at a higher voltage (6 V). Likewise, the DC bias has no current flow since the capacitors act as open circuits and prevent transmission of the DC signal to the beam. Therefore, the off-resonant current out of the drain is simply the AC signal attenuated by the resistance of the beam. Computing the static beam resistance from Equation (2.19), and using Ohm's law to compute the output voltage develops a result slightly larger than predicted by the simulation. This is reasonable when the static deflection present in the beam due to the DC bias is considered. The added deflection will increase the piezoresistance according to Equation (2.19) and correspondingly decrease the output current. Near resonance, the beam motion creates fluctuations in the resistance and capacitance. The oscillation in the beam resistance leads to both larger and smaller resistances, but, from an average perspective, the RMS value of the resistance is increasing as resonance is approached. Therefore, it is reasonable to assume that the output current will decrease as the resonant frequency is approached. The motional capacitance allows some of the DC bias to generate small currents flowing from the gate to the beam. It is interesting to consider the implications of the nonlinearity of the system, especially with regard to the generation of other frequency components. While the input frequency will commonly see a larger off-resonant current and an antiresonance, a harmonic or mixed-frequency component would see a small off-resonant current, as the motion of the beam would be too small to produce harmonic signals. The extra frequency component would only have more amplitude near resonance where the motional effects allow for generation of these terms. Therefore it is reasonable to expect an antiresonance in one frequency component but a resonance in another harmonic at the same time. Indeed, this is what is observed in Section 5.1.

In Case 2, the AC signal cannot reach the output port at any frequency because the beam's midpoint voltage is greater than the amplitude of the AC signal. Thus the magnitude of the output current is dependent solely on the modulation of the DC biases through the piezoresistive effects, and the AC signal controls the vibration of the beam defining that modulation. The capacitive interaction serves only to leach current from the beam to the lower potential gate. Off-resonant frequencies generate little motion, and therefore there is negligible harmonic content in the output. Near-resonant inputs allow the modulation of the DC bias to generate AC currents, and despite the current lost to the gate, the output sees a peak current at resonance for its harmonic content. If the DC content of the output current was observed, it would be expected that there would be an antiresonance with a larger off-resonance current, similar to that observed for Case 1.

Cases 3 and 4 combine the AC and DC signals on a single input, and can be considered as opposite loading conditions for the same circuit. Considering Case 3 in off-resonant loading, only the AC component of the signal will traverse the capacitance, after attenuation by half of the beam resistance. This will produce only a small off-resonance current, but it will be larger than that in Case 2, which has no direct AC contribution. Near-resonant currents will increase, as the RMS capacitance increases according to Equation (2.10). The increase in capacitance will correspondingly increase the output current following a capacitor's current-voltage relation, Equation (2.13). A slight current addition from the DC bias on the drain can also be relied upon to increase the output current through the motional capacitance term. When the circuit is reversed, the same effects are achieved, since the capacitive and resistive elements are in series.

To adjust from Cases 3 and 4 to the coupled cases, 5 and 6, it is only necessary to consider both halves of the beam's resistance as being in parallel, instead of focusing on only one half. Ultimately this reduces the effective resistance, allowing for a larger output current. A smaller effective resistance also implies that more of the voltage drop occurs across the beam-gate capacitance, resulting in a larger forcing voltage and thus more displacement, cascading into a larger capacitance and capacitive current. The increased capacitive current would be balanced by an accompanying increase in the RMS resistance for the beam. However, in comparison to Cases 3 and 4, the decreased resistance arising from treating the two halves of the beam resistance in parallel means that the dominant effect will be to see a larger peak current flow. In each case, these predictions align with the shape and amplitude order revealed through the simulation.

Each set of cases saw a distinct frequency, as correlated in Table 6.2. This phenomena is predicted by the analysis presented in Section 5.2. Since the geometry and residual stress are not changing between each configuration, it must be the electrostatic terms alone that are altering the response location. The voltage in question here is the potential across the beam-gate capacitor. Once again, let $V(t)$ be approximated by $V = V_{rms}$. For Case 1, the DC bias forms a constant 6 V potential on one side, and the 40 mV$_{rms}$ AC input provides a 20 mV$_{rms}$ potential on the other, leading to a maximum voltage of 6.02 V$_{rms}$. Similarly, Case 2 has a constant 40 mV_{rms} AC signal on one side of the capacitor, and a 3 V DC potential on the beam side due to the beam resistance. The 3.04 V_{rms} voltage for Case 2 will result in less electrostatic softening and result in a higher resonance frequency than Case 1. This prediction matches what is observed in the simulation. The single path excitation Cases, 3 through 6, are more challenging to compare with Cases 1 and 2, since the forcing voltage is tied to the current through the entire path. It should again be noted that the actual resonance location is clearly dependent on the nonlinear terms in the beam equations, and the forcing voltage is also coupled to the piezoresistive effects and the various capacitive effects, making a precise prediction of its location difficult, as shown in Section 5.2. This is why the prediction for a larger forcing voltage in Cases 5 and 6, as compared to Cases 3 and 4, can be accurate while 5 and 6 show a larger peak frequency.

6.2 Development of Systems for Self-Oscillation

The potential to develop small, on-chip frequency sources is a very attractive draw of M/NEMS. Stable frequency sources can be used in applications ranging from clock signals to mass sensors. While quartz crystals are cheap and prolific, the potential to miniaturize and integrate oscillators on chip is clearly appealing. Several previous efforts have already successfully shown MEMS devices that can operate as self-oscillators with the proper feedback arrangement [4, 68–70].

6.2.1 Circuit Design

To investigate the potential of the nanoresonators for use as self-oscillators, a simulation was created to directly excite the device model, simulating an on-chip set-up rather than the probe station testing used in the experimentation. The simulation used a 1 kΩ resistor to ground on the source node in order to consider a voltage output. The simulation allowed the rapid testing of several input/output configurations to optimize the layout. Based on observations from prior work [69, 70], the primary layout placed a DC bias on the back gate to tension the beam and cause an initial transient vibration that was nourished into a sustained oscillation through the feedback loop. Other layouts were investigated, but combinations were restricted by the desire to avoid needing to implement a bias-tee to those that isolate DC and AC signals on different ports.

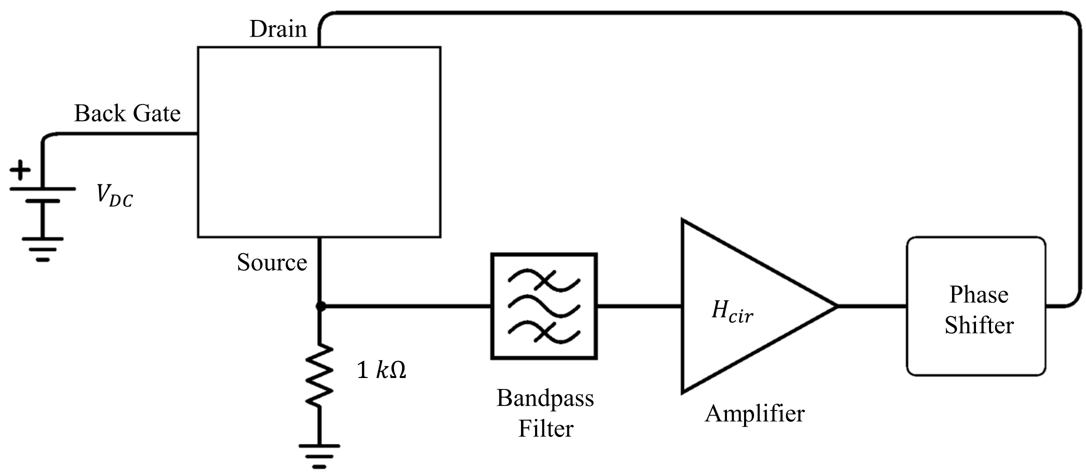

Figure 6.3. The circuit schematic for the primary feedback system investigated. The output was considered to be the voltage across the 1 kΩ resistor.

The simulations focused on a 6.3 μm long beam with a 120 nm wide by 110 nm tall cross-section. All other parameters were kept constant with those used in the Table 4.1. The feedback setup had four primary settings that could be tuned, besides the circuit layout. The filter pass band (center frequency and relative bandwidth), the amplifier gain, and the phase shift. Note that within the simulation, the phase shift was set by adjusting a desired frequency. However, testing revealed that the set frequency receives a $-133°$ phase shift through the shifter instead of $-90°$ as might be expected. Therefore, the set frequency was raised to create a constant $-90°$ phase shift up to at least 4ω. While this wide band is not a direct representation of a physical system, the filtering of the feedback signal implies that only the phase shift around the passband is relevant in any simulation. This allows the wideband to be considered relevant for multiple filter frequencies.

6.2.2 Simulated Response

Of the different input and feedback configurations tested, the case pictured in Figure 6.3, and described above, produced the best oscillation for the smallest gains. The following comments are relevant to that circuit layout.

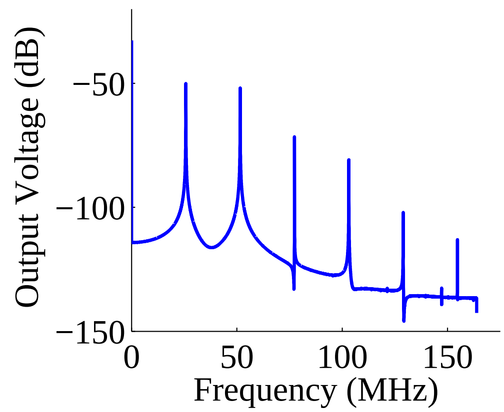

Figure 6.4. The output spectrum across the 1 kΩ resistor without any filtering in the feedback loop. $H_{cir} = 40.4785$ dB (109x).

The nonlinearities of the resonator inherently produce multiple frequencies within the output voltage. Therefore, initial feedback attempts resulted in a steady oscillation with a dominant fundamental frequency of 25.2718 MHz, but with many higher harmonics also present, as seen in Figure 6.4. In order to restrict the final output to a single frequency, a filter was used prior to the amplifier. Figure 6.5 shows that the filter can successfully select which frequency dominates the output of the oscillator. Each harmonic requires a slightly different gain setting to achieve a stable output. The variation in the required gain can be attributed to the small initial amplitude for the mixing-generated higher harmonic terms, which will require more gain to achieve a stable oscillation.

The initial gain needed in the feedback loop was estimated using a transient response from a DC step input with no feedback loop present. Referencing the peak

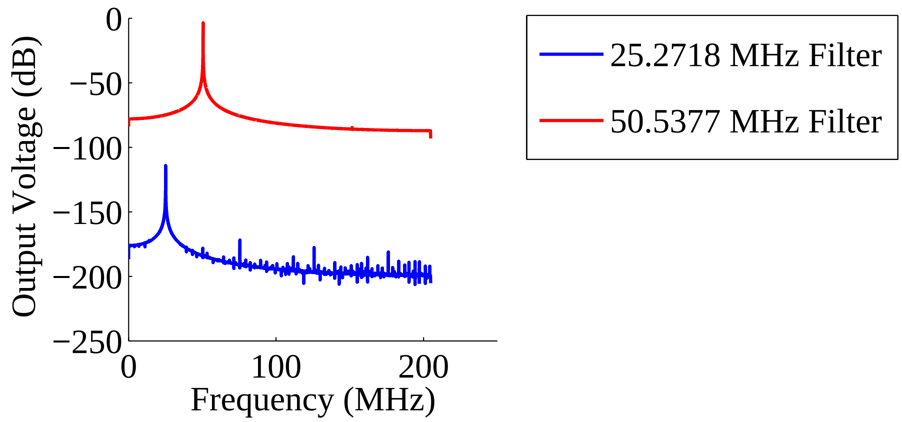

Figure 6.5. Spectrum of the voltage output across the 1 kΩ resistor for ω and 2ω filters in the feedback loop. Note that the 2ω response is likely to result in pull-in. $H_{cir,\omega} = 41.7981$ dB (122x), $H_{cir,2\omega} = 41.5836$ dB (120x).

output amplitude to the initial DC voltage gave some measure of the system attenuation. Using the amplitude condition of the Barkhausen stability criterion [68],

$$|H_{res} \times H_{cir}|_{f_{osc}} > 1 \qquad \angle|H_{res} \times H_{cir}| = 0°, \tag{6.1}$$

the feedback gain could be selected to counteract the attenuation. This method correctly predicted how much feedback gain would be needed, before the filter was added. However, the initial transient measurement does not provide an estimate of the phase shift required to meet the phase condition, because there is no AC input reference. In the absence of an estimate, the simulations initially used a 90° phase lag in correspondence with what was shown to be successful in prior work [68–70]. Other phase lags were tested, and those near 90° and 270° would produce sustained oscillations. This corresponds with the idea that the phase shift within the resonator is rooted in capacitive interaction and harmonic mixing, which inherently produce 90° shifts. It was noted that slight variations in the phase shift would produce different oscillating frequencies. Reference [68] suggests that

$$f_{osc} = f_r \left(1 + \frac{\Delta\psi}{2Q}\right), \tag{6.2}$$

where $\Delta\psi$ is the phase shift beyond what is needed to reach the Barkhausen criteria, in this case $-90°$, f_r is the nominal resonance frequency, and Q is the quality factor of the resonator which is a measure of the system's damping. This explains the frequency-phase link and could potentially provide a methodology for quantifying the damping of the nanoresonators, assuming the nominal resonant frequency as known.

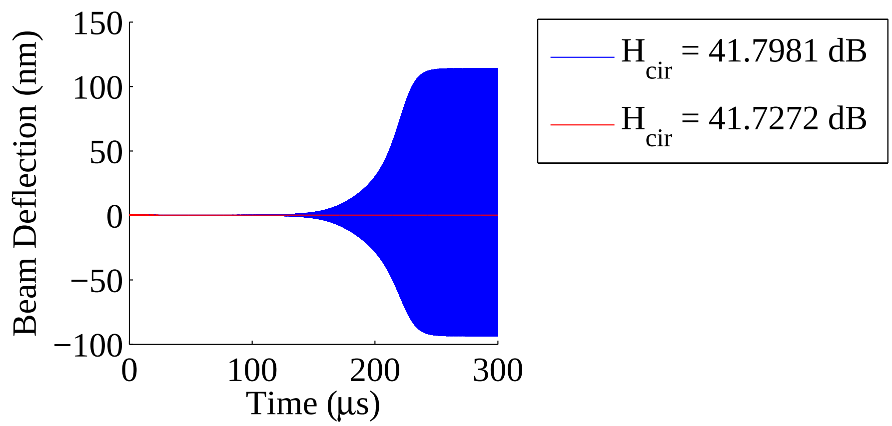

Figure 6.6. The change in the transient beam deflection due to a slight increase in feedback gain. The smaller oscillation is negligible in comparison to the larger oscillation, which is assumed to represent pull-in.

Theoretically, the amplifier gain could be increased to achieve a larger output signal. Under practical conditions, the resonator quickly runs into issues with forcing voltages that produce pull-in effects. Because the resonator model expands the electrostatic forcing around $z(t) = 0$, the model does not accurately predict responses for large amplitude deflections (see Section 2.5). If the common $1/3$ rule of static pull-in is implemented and it is, rather conservatively, considered that pull-in will occur when the beam deflects to $1/3$ of the gap distance, then a threshold for which simulations can be assumed to be valid or not is created. For the standard 144 nm gap on these devices, this gives a maximum valid simulation displacement of 48 nm. This proves to be a very limiting cut-off, and severely restricts the viable inputs and gains. Table 6.4 shows the final combinations that produce a sustained oscillation. Figure 6.6 shows that changing from a gain of 41.7272 dB (122x) to 41.7981 dB (123x) creates a large difference in the beam deflection for a first harmonic, 2 V_{DC} test case. On the other hand, too little gain allows the transient response to quickly dissipate. Increasing the DC bias also increases the amplitude of the beam displacement, resulting in no gain that satisfactorily creates oscillation without pull-in for a 3 V_{dc} step input and higher. Excitation at the second harmonic has a more restricted set of working frequencies, because of the need for a larger gain to overcome the smaller initial amplitude and due to the static beam deflection at steady state.

Table 6.4. Required Circuit Gains.

DC Bias	1^{st} Harmonic Gain (dB)
1	42.3454 – 42.4770 (131x-133x)
2	41.7272 (122x)
3	*N/A*

Due to the narrow ranges of viable gains and input power, along with the very small power output of the devices, there appears to be few benefits to further pursuing the use of these devices as self-oscillators, since other devices have already shown a higher propensity for use in this field [4, 51].

6.3 A Study of Coupled Devices

While the coupling of the beam displacement with the electrostatic dynamics of the beam voltage drastically increases the difficulty and effort required to analytically analyze a single nanoresonator, the combination of even two of the systems would prove extremely difficult to analyze. It is under these circumstances that the power of the simulation shines. It is no more difficult to compute the response of two or more devices than it is for a single device. From a design standpoint, there are many situations where the combination of multiple devices could be beneficial. The ability to design an on-chip filter using a combination of devices in both the pass- and stop-band configurations seen in Section 6.1 would allow a designer to create very precise filter responses.

The simulation was used to analyze the effects of directly connecting two of the beam systems, each excited by a common back gate. This accurately represents the case for the majority of nanobeams that would be fabricated on chip, since there is only one back gate substrate layer that all devices interact with. The exception to this would be a chip of devices that were all fabricated to be actuated in-plane, in which case each side gate could be independently biased. Both nanobeams matched the parameters listed in Table 4.1, with a width of 120 nm. The length of each beam was varied to study the effects of changing the natural frequencies on the final output power. In order to provide each nanobeam with similar amounts of harmonic forcing, the AC signal was applied to the back gate, while the DC bias was contributed through the drain of the first nanoresonator. The second nanoresonator then receives the same AC gate signal while also receiving both an AC and DC signal through its drain. Therefore, the final response is not simply a product of the two resonant frequencies, but also the order in which they are placed in the final filter setup. Figure 6.7 depicts this layout.

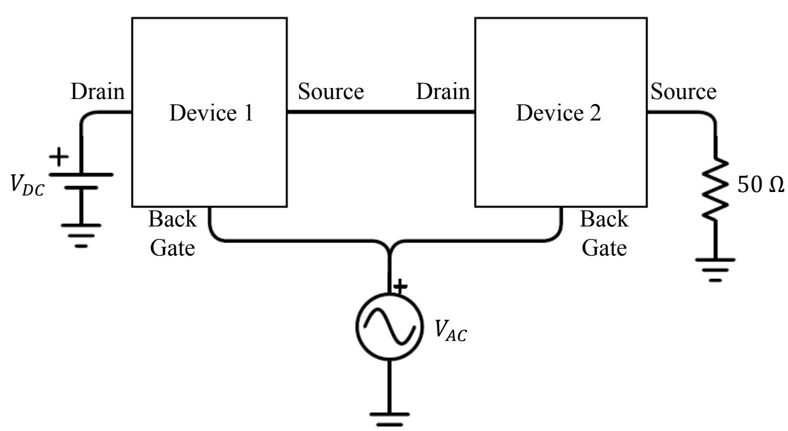

Figure 6.7. Circuit layout for a series connection of two nanoresonators which exhibits a coupling effect when the resonant frequencies are similar to each other.

When the lengths of the beam are different, such that the resonances are sufficiently separated, then the net system response features two separate resonant peaks, as seen in Figure 6.8. Here the amplitude of the first beam's vibration is larger than that of the second. As the length of the second beam approaches 6 μm, the peaks begin to overlap, producing a joint resonance of a greater bandwidth, see Figure 6.9. Finally, as the natural frequencies become closer, the system output becomes a single pass-band, with one section of increased amplitude where both resonances overlap. It is interesting to note that in the case of Figure 6.10, the amplitude of the second beam is now dominant over that of the first beam, and that both resonances exhibit their bifurcation at the same frequency. The second beam's response is bifurcating sooner than would be predicted from the previous cases, and results in a narrower passband for the overall system.

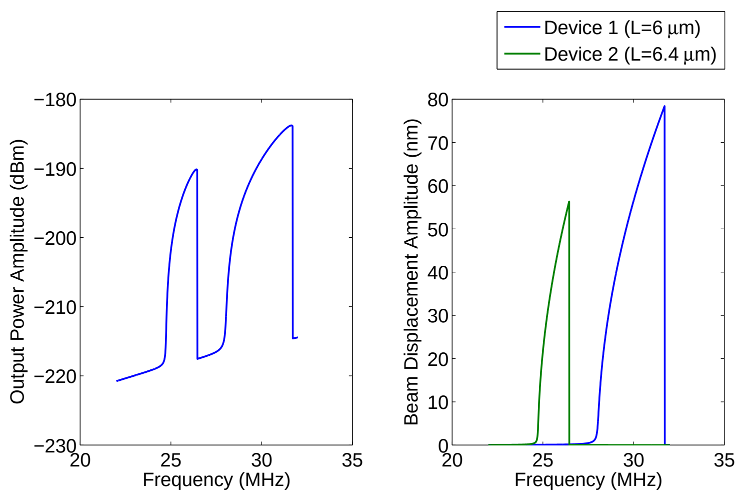

Figure 6.8. The output power across a 50 Ω resistor (left) and beam displacements (right) for a series of nanoresonator systems. The devices were actuated using $V_{D,1} = 6$ V$_{dc}$ and $V_{b,1,2} = 40$ mV$_{rms}$.

If the lengths are reciprocated and kept within 1 μm, the second device now exhibits the larger vibration, with the same system output response. Interestingly, as the length of the first beam is now increased, the system response remains coupled (Figure 6.12) until a larger difference in lengths is achieved than was require for

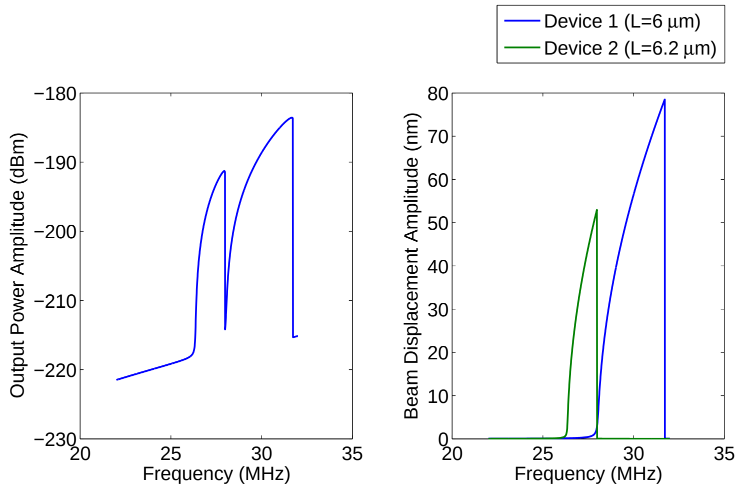

Figure 6.9. The output power across a 50 Ω resistor (left) and beam displacements (right) for a series of nanoresonator systems. The devices were actuated using $V_{D,1} = 6$ V$_{dc}$ and $V_{b,1,2} = 40$ mV$_{rms}$.

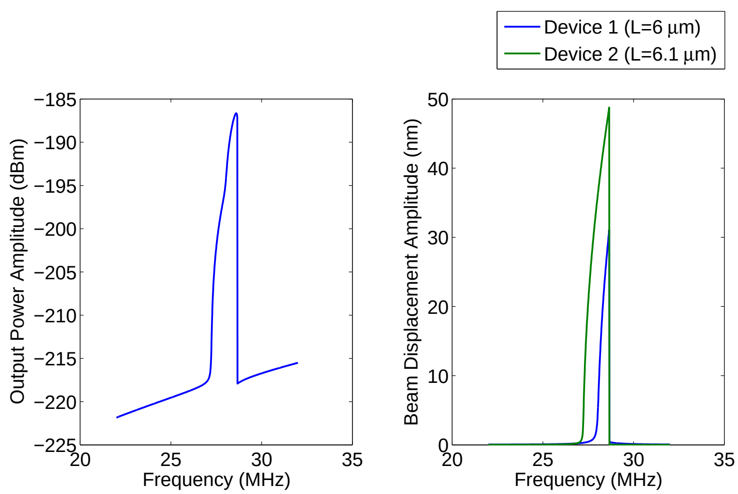

Figure 6.10. The output power across a 50 Ω resistor (left) and beam displacements (right) for a series of nanoresonator systems. The devices were actuated using $V_{D,1} = 6$ V$_{dc}$ and $V_{b,1,2} = 40$ mV$_{rms}$.

separation when beam 1 was larger than beam 2 (Figure 6.13). Throughout all of this second set of responses, the first beam has maintained the larger amplitude displacement. Until the beam resonances have moved far enough apart to decouple the system resonance, both nanobeams bifurcate at the same frequency. This behavior occurs in Figure 6.12, despite the lack of response coupling for the reciprocal beam arrangement in Figure 6.9. In this coupled case, neither beam reaches the same peak displacement as when decoupled, bifurcating at a frequency in between both of the peak frequencies observed in Figure 6.9.

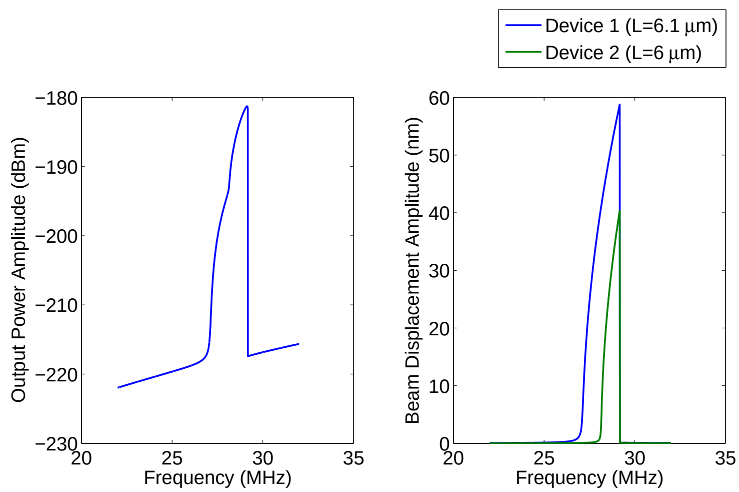

Figure 6.11. The output power across a 50 Ω resistor (left) and beam displacements (right) for a series of nanoresonator systems. The devices were actuated using $V_{D,1} = 6$ V$_{dc}$ and $V_{b,1,2} = 40$ mV$_{rms}$.

It is proposed that the coupling effect arises when the start of a resonator's pass-band begins within the pass-band of the other. As the length of the second beam decreases to match that of the first beam (Figures 6.8 through 6.10), the response is only coupled once the first beam's pass-band begins inside of the pass-band of the second resonator. Similarly, as the length of the first beam increases away from the length of the second beam (Figures 6.11 through 6.13), the responses continue to bifurcate together until the length of the first beam is sufficient to drop the resonance low enough that the pass-band of the second beam no longer begins within the pass-band of the first. It is reasonable to consider that when one of the systems begins its resonance under a loading defined by the resonant amplitude of the other device, that when the initial resonant system bifurcates, the transition is enough to ruin the stability of the other system. The difference between Figure 6.11 and Figure

6.13 shows that the systems can exhibit a strong relation between the electrical and mechanical responses, as when they are bifurcating and producing a joined system resonance in Figure 6.11. Or, they may exhibit relatively independent responses, as is the case in Figure 6.13, where the system has an electrical resonance corresponding to each of the nanoresonators, but neither beam increases in amplitude during the other's resonance, and the mechanical resonances of each subsystem seem to be independent of the other.

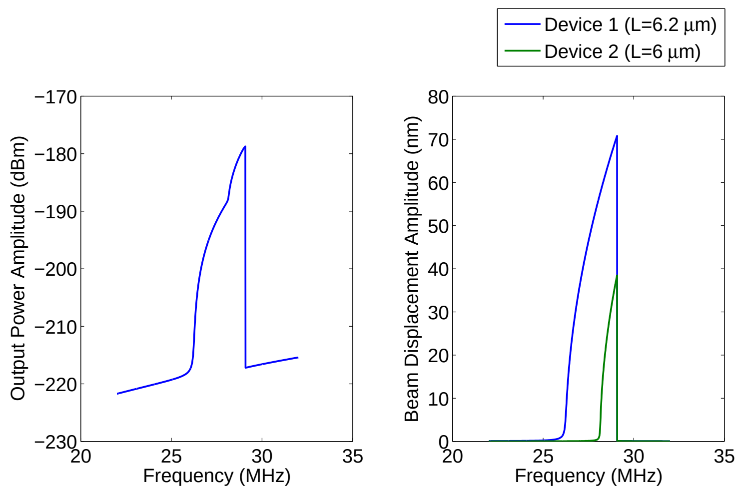

Figure 6.12. The output power across a 50 Ω resistor (left) and beam displacements (right) for a series of nanoresonator systems. The devices were actuated using $V_{D,1} = 6$ V$_{dc}$ and $V_{b,1,2} = 40$ mV$_{rms}$.

With these results, it may be possible to create a series of nanoresonators in order of increasing frequency to create a much broader pass-band. Alternatively, these phenomena could be utilized to increase the reliability of a chip design. By designing a series of coupled devices of the same length, any tolerance issues should be mitigated by the coupling of the net response to an average near the desired response.

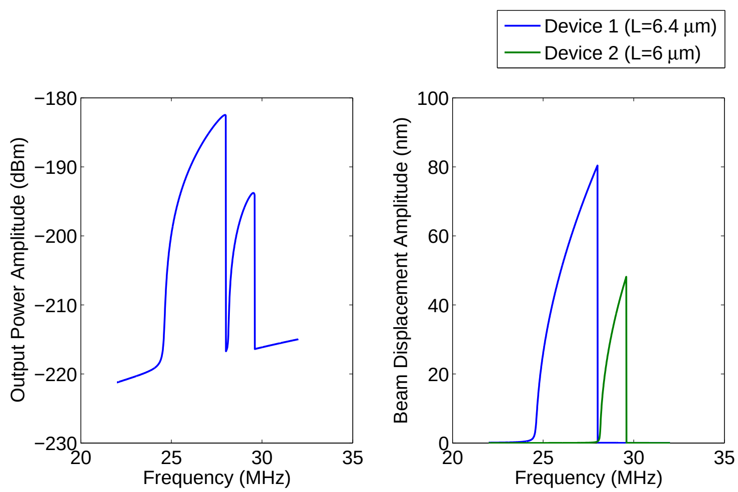

Figure 6.13. The output power across a 50 Ω resistor (left) and beam displacements (right) for a series of nanoresonator systems. The devices were actuated using $V_{D,1} = 6$ V$_{dc}$ and $V_{b,1,2} = 40$ mV$_{rms}$.

CHAPTER 7. CONCLUSION

It was shown that the mechanical nature of the nanobeam system can be modeled using a Bernoulli-Euler beam model with mid-plane stretching and residual stress. The electrical architecture of the system can be modeled using a combination of variable resistors and capacitors, whose values are linked to the deformation of the beam. This provides a system of equations determining the beam deflection and voltage.

Experimental data was collected on a prototypical device in Chapter 3, and used to qualitatively validate the performance of the model in Chapter 4. The system's equivalent circuit was simulated and studied to provide insight into the possible practical applications of the nanoresonator. A study relating the application of the AC and DC signals to the output of the system and whether it displays a resonant or anti-resonant response was presented in Section 6.1. It was also shown that the electrical power provided to the system tunes the resonant frequency in Sections 5.1, 5.2, and 6.1. This is given as grounds for recommending against the use of mixing methodologies in experimentation, since the simulation shows great discrepancies between the observed output in this case and a measurement taken directly at the excitation frequency.

The mathematical system was used to predict the tuned, linear, natural frequency in Section 5.2, but the simulation shows that this only accurately predicts the tuning behavior of the down-sweep resonance. The hardening response results in a peak frequency greater than what is predicted by the natural frequency. The nonlinearities and displacement-voltage interactions lead to a different tuning behavior than predicted for the up-sweep responses. In Section 5.3, the difficulties of achieving a softening response for a beam with a dominant cubic nonlinearity were explored, and it was suggested that an initially curved beam would be beneficial to achieving a design that could alternate between a hardening and softening response backbone.

Further case studies were also used to demonstrate possible applications of the devices, such as a filter or self-oscillator. Section 6.2 demonstrated that while the system is easily capable of achieving self-oscillation, the feedback requires a very narrow band of large amplifications to produce a small output signal. Therefore it is proposed that the devices not be considered for this use. It was proposed in Section 6.3 that using multiple resonators in series could serve as a method to overcome fabrication tolerances through the coupling of their responses.

LIST OF REFERENCES

LIST OF REFERENCES

[1] A. K. Huttel, G. A. Steele, B. Witkamp, M. Poot, L. P. Kouwenhoven, and H. S. J van der Zant. Carbon nanotubes as ultrahigh quality factor mechanical resonators. *Nano Letters*, 9(7):2547–2552, 2009.

[2] K. Chen, X. Liu, A. Kovacs, W. J. Chappell, and D. Peroulis. Antibiased electrostatic RF MEMS varactors and tunable filters. *IEEE Transactions on Microwave Theory and Techniques*, 58(12):3971–3981, 2010.

[3] A. Bachtold, P. Hadley, T. Nakanishi, and C. Dekker. Logic circuits with carbon nanotube transistors. *Science*, 294(5545):1317–1320, 2001.

[4] X. L. Feng, C. J. White, A. Hajimiri, and M. L. Roukes. A self-sustaining ultrahigh-frequency nanoelectromechanical oscillator. *Nature Nanotechnology*, 3(6):342–346, 2008.

[5] J. Chaste, L. Lechner, P. Morfin, G. Feve, T. Kontos, J.-M. Berroir, D.C. Glattli, H. Happy, P. Hakonen, and B. Placais. Single carbon nanotube transistor at GHz frequency. *Nano letters*, 8(2):525–528, 2008.

[6] D. Grogg and A. M. Ionescu. The vibrating body transistor. *IEEE Transactions on Electron Devices*, 58(7):2113–2121, 2011.

[7] M. Koskenvuori and I. Tittonen. Towards micromechanical radio: Overtone excitations of a microresonator through the nonlinearities of the second and third order. *Journal of Microelectromechanical Systems*, 17(2):363–369, 2008.

[8] V. Gouttenoire, T. Barois, S. Perisanu, J.-L. Leclercq, S. T. Purcell, P. Vincent, and A. Ayari. Digital and FM demodulation of a doubly clamped single-walled carbon-nanotube oscillator: Towards a nanotube cell phone. *Small*, 6(9):1060–1065, 2010.

[9] B. Lassagne, D. Garcia-Sanchez, A. Aguasca, and A. Bachtold. Ultrasensitive mass sensing with a nanotube electromechanical resonator. *Nano Letters*, 8(11):3735–3738, 2008.

[10] J. Arcamone, M. Sansa, J. Verd, A. Uranga, G. Abadal, N. Barniol, M. van den Boogaart, J. Brugger, and F. Perez-Murano. Nanomechanical mass sensor for spatially resolved ultrasensitive monitoring of deposition rates in stencil lithography. *Small*, 5(2):176–180, 2009.

[11] E. Forsen, G. Abadal, S. Ghatnekar-Nilsson, J. Teva, J. Verd, R. Sandberg, W. Svendsen, F. Perez-Murano, J. Esteve, E. Figueras, F. Campabadal, L. Montelius, N. Barniol, and A. Boisen. Ultrasensitive mass sensor fully integrated with complementary metal-oxide-semiconductor circuitry. *Applied Physics Letters*, 87(4):043507, 2005.

[12] J. Chaste, A. Eichler, J. Moser, G. Ceballos, R. Rurali, and A. Bachtold. A mechanical mass sensor with yoctogram resolution. *Nature Nanotechnology*, 7(5):301–304, 2012.

[13] J. L. Lopez, J. Verd, J. Teva, G. Murillo, J. Giner, F. Torres, A. Uranga, G. Abadal, and N. Barniol. Integration of RF-MEMS resonators on submicrometric commercial CMOS technologies. *Journal of Micromechanics and Microengineering*, 19(1):015002, 2009.

[14] L. Yu, H. Pajouhi, M. R. Nelis, J. F. Rhoads, and S. Mohammadi. Tunable, dual-gate, silicon-on-insulator (SOI) nanoelectromechancial resonators. *IEEE Transactions on Nanotechnology*, 11(6):1093–1099, 2012.

[15] J. Teva, G. Abadal, A. Uranga, J. Verd, F. Torres, J. L. Lopez, J. Esteve, F. Perez-Murano, and N. Barniol. From VHF to UHF CMOS-MEMS monolithically integrated resonators. In *Proceedings of the IEEE 21st International Conference on Micro Electro Mechanical Systems (MEMS)*, pages 82–85. IEEE, 2008.

[16] E. Ollier, C. Dupre, G. Arndt, J. Arcamone, C. Vizioz, L. Duraffourg, E. Sage, A. Koumela, S. Hentz, G. Cibrario, P. Meininger, K. Benotmane, C. Marcoux, O. Rozeau, G. Billiot, E. Colinet, F. Andrieu, J. Philippe, F. Aussenac, D. Mercier, H. Blanc, T. Ernst, and P. Robert. Ultra-scaled high-frequency single-crystal Si NEMS resonators and their front-end co-integration with CMOS for high sensitivity applications. In *Procedings of the IEEE 25th International Conference on Micro Electro Mechanical Systems (MEMS)*, pages 1368–1371. IEEE, 2012.

[17] X. M. H. Huang, C. A. Zorman, M. Mehregany, and M. L. Roukes. Nanodevice motion at microwave frequencies. *Nature*, 421(6922):496–497, 2003.

[18] S. Krylov and S. Serentensky. Higher order correction of electrostatic pressure and its influence on the pull-in behavior of microstructures. *Journal of Micromechanics and Microengineering*, 16(7):1382–1396, 2006.

[19] B. Bhushan and G. B. Agrawal. Stress analysis of nanostructures using a finite element method. *Nanotechnology*, 13(4):515–523, 2002.

[20] E. Hamad and A. Omar. An improved two-dimensional coupled electrostatic-mechanical model for RF MEMS switches. *Journal of Micromechanics and Microengineering*, 16(7):1424–1429, 2006.

[21] C. O'Mahony, M. Hill, R. Duane, and A. Mathewson. Analysis of electromechanical boundary effects on the pull-in of micromachined fixed–fixed beams. *Journal of Micromechanics and Microengineering*, 13(4):S75–S80, 2003.

[22] F. Tay, X. Jun, Y. Liang, V. J. Logeeswaran, and Y. Yufeng. The effects of non-parallel plates in a differential capacitive microaccelerometer. *Journal of Micromechanics and Microengineering*, 9(4):283–293, 1999.

[23] A. N. Cleland. Thermomechanical noise limits on parametric sensing with nanomechanical resonators. *New Journal of Physics*, 7(235):1–16, 2005.

[24] J. A. Judge, D. M. Photiadis, J. F. Vignola, B. H. Houston, and J. Jarzynski. Attachment loss of micromechanical and nanomechanical resonators in the limits of thick and thin support structures. *Journal of Applied Physics*, 101(1):013521, 2007.

[25] J. A. Judge, J. F. Vignola, and J. Jarzynski. Dissipation from microscale and nanoscale beam resonators into a surrounding fluid. *Applied Physics Letters*, 92(12):124102, 2008.

[26] S. Ai and J. A. Pelesko. Dynamics of a canonical electrostatic MEMS/NEMS system. *Journal of Dynamics and Differential Equations*, 20(3):609–641, 2008.

[27] W. G. Conley, A. Raman, C. M. Krousgrill, and S. Mohammadi. Nonlinear and non-planar dynamics of suspended nanotube and nanowire resonators. *Nano Letters*, 8(6):1590–1595, 2008.

[28] A. Vyas, A. K. Bajaj, A. Raman, and D. Peroulis. Nonlinear micromechanical filters based on internal resonance phenomenon. In *Proceedings of the Topical Meeting on Silicon Monolithic Integrated Circuits in RF Systems*, pages 35–38. IEEE, 2006.

[29] R. C. Batra, M. Porfiri, and D. Spinello. Review of modeling electrostatically actuated microelectromechanical systems. *Smart Materials and Structures*, 16(6):R23–R31, 2007.

[30] R. Lifshitz and M. L. Roukes. Thermoelastic damping in micro- and nanomechanical systems. *Physical Review B*, 61(8):5600–5609, 2000.

[31] E. M. Abdel-Rahman, M. I. Younis, and A. H. Nayfeh. Characterization of the mechanical behavior of an electrically actuated microbeam. *Journal of Micromechanics and Microengineering*, 12(6):759–766, 2002.

[32] H. M. Ouakad and M. I. Younis. Nonlinear dynamics of electrically actuated carbon nanotube resonators. *Journal of Compuational and Nonlinear Dynamics*, 5(1):011009, 2009.

[33] A. Eichler, J. Moser, J. Chaste, M. Zdrojek, I. Wilson-Rae, and A. Bachtold. Nonlinear damping in mechanical resonators made from carbon nanotubes and graphene. *Nature Nanotechnology*, 6(6):339–342, 2011.

[34] A. Uranga, J. Verd, E. Marigo, J. Giner, J. L. Munoz-Gamarra, and N. Barniol. Exploitation of non-linearities in CMOS-NEMS electrostatic resonators for mechanical memories. *Sensors and Actuators A: Physical*, 197(0):88–95, 2013.

[35] D. Garcia-Sanchez, A. San Paulo, M. J. Esplandiu, F. Perez-Murano, L. Forró, A. Aguasca, and A. Bachtold. Mechanical detection of carbon nanotube resonator vibrations. *Physical Review Letters*, 99(8):085501, 2007.

[36] A. Uranga, J. Verd, J. L. Lopez, J. Teva, G. Abadal, F. Torres, J. Esteve, F. Perez-Murano, and N. Barniol. Fully integrated mixler based on VHF CMOS-MEMS clamped-clamped beam resonator. *Electronics Letters*, 43(8):452–454, 2007.

[37] R. N. Candler, H. Li, M. Lutz, W.-T. Park, A. Partridge, G. Yama, and T. W. Kenny. Investigation of energy loss mechanisms in micromechanical resonators. In *Proceedings of the 12th International Conference on Solid-State Sensors, Actuators and Microsystems*, volume 1, pages 332–335. IEEE, 2003.

[38] K. Y. Yasumura, T. D. Stowe, E. M. Chow, T. Pfafman, T. W. Kenny, B. C. Stipe, and D. Rugar. Quality factors in micron- and submicron-thick cantilevers. *Journal of Microelectromechanical Systems*, 9(1):117–125, 2000.

[39] V. Sazonova, Y. Yaish, H. Ustunel, D. Roundy, T. A. Arias, and P. L. McEuen. A tunable carbon nanotube electromechanical oscillator. *Nature*, 431(7006):284–287, 2004.

[40] A. Sabater, V. Kumar, A. Mahmood, and J. F. Rhoads. On the nonlinear dynamics of electromagnetically transduced microresonators. *Journal of Microelectromechanical Systems*, 22(5):1020–1031, 2013.

[41] R. He, X. L. Feng, M. L. Roukes, and P. Yang. Self-transducing silicon nanowire electromechanical systems at room temperature. *Nano Letters*, 8(6):1756–1761, 2008.

[42] P. A. Truitt, J. B. Hertzberg, E. Altunkaya, and K. C. Schwab. Linear and nonlinear coupling between transverse modes of a nanomechanical resonator. *Journal of Applied Physics*, 114(11):114307, 2013.

[43] A. T. H. Lin, J. E. Y. Lee, J. Yan, and A. A. Seshia. Methods for enhanced electrical transduction and characterization of micromechanical resonators. *Sensors and Actuators A: Physical*, 158(2):263–272, 2010.

[44] M. Koskenvuori and I. Tittonen. Improvement of the conversion performance of a resonating multimode microelectromechanical mixer-filter through parametric amplification. *IEEE Electron Device Letters*, 28(11):970–972, 2007.

[45] B. Witkamp, M. Poot, and H. S. J. van der Zant. Bending-mode vibration of a suspended nanotube resonator. *Nano Letters*, 6(12):2904–2908, 2006.

[46] R. He and P. Yang. Giant piezoresistance effect in silicon nanowires. *Nature Nanotechnology*, 1(1):42–46, 2006.

[47] H. W. C. Postma, I. Kozinsky, A. Husain, and M. L. Roukes. Dynamic range of nanotube- and nanowire-based electromechanical systems. *Applied Physics Letters*, 86(22):223105, 2005.

[48] I. Kozinsky, H. W. C. Postma, I. Bargatin, and M. L. Roukes. Tuning nonlinearity, dynamic range, and frequency of nanomechanical resonators. *Applied Physics Letters*, 88(25):253101, 2006.

[49] G. K. Fedder and Q. Jing. A hierarchical circuit-level design methodology for microelectromechanical systems. *IEEE Transactions on Circuits and Systems II: Analog and Digital Signal Processing*, 46(10):1309–1315, 1999.

[50] T. Mukherjee, G. K. Fedder, D. Ramaswamy, and J. White. Emerging simulation approaches for micromachined devices. *IEEE Transactions on Computer-Aided Design of Integrated Circuits and Systems,*, 19(12):1572–1589, 2000.

[51] E. Colinet, L. Duraffourg, S. Labarthe, S. Hentz, P. Robert, and P. Andreucci. Self-oscillation conditions of a resonant nanoelectromechanical mass sensor. *Journal of Applied Physics*, 105(12):124908, 2009.

[52] F. Chen, J. Brotz, U. Arslan, C. C. Lo, T. Mukherjee, and G. K. Fedder. CMOS-MEMS resonant RF mixer-filters. In *Proceedings of the IEEE 18th International Conference on Micro Electro Mechanical Systems (MEMS)*, pages 24–27, 2005.

[53] J. A. Pelesko and T. A. Driscoll. The effect of the small-aspect-ratio approximation on canonical electrostatic MEMS models. *Journal of Engineering Mathematics*, 53(3-4):239–252, 2005.

[54] M. I Younis. *MEMS Linear and Nonlinear Statics and Dynamics*, volume 20. Springer, 2011.

[55] H. M. Ouakad and M. I. Younis. Natural frequencies and mode shapes of initially curved carbon nanotube resonators under electric excitation. *Journal of Sound and Vibration*, 330(13):3182–3195, 2011.

[56] F. R. Blom, S. Bouwstra, M. Elwenspoek, and J. H. J. Fluitman. Dependence of the quality factor of micromachined silicon beam resonators on pressure and geometry. *Journal of Vacuum Science and Technology B*, 10(1):19–26, 1992.

[57] V. B. Braginsky, V. P. Mitrofanov, and V. I. Panov. *Systems with Small Dissipation*. The University of Chicago Press, Chicago, 1985.

[58] R. C. Batra, M. Porfiri, and D. Spinello. Capacitance estimate for electrostatically actuated narrow microbeams. *Micro Nano Letters, IET*, 1(2):71–73, 2006.

[59] B. E. DeMartini, J. F. Rhoads, K. L. Turner, S. W. Shaw, and J. Moehlis. Linear and nonlinear tuning of parametrically excited MEMS oscillators. *Journal of Microelectromechanical Systems*, 16(2):310–318, 2007.

[60] N. Kacem, S. Baguet, S. Hentz, and R. Dufour. Pull-in retarding in nonlinear nanoelectromechanical resonators under superharmonic excitation. *Journal of Computational and Nonlinear Dynamics*, 7(2):021011, 2012.

[61] Y. Kanda. A graphical representation of the piezoresistance coefficients in silicon. *IEEE Transactions on Electron Devices*, 29(1):64–70, 1982.

[62] J. Chen, S.-M. Kang, J. Zou, C. Liu, and J. E. Schutt-Aine. Reduced-order modeling of weakly nonlinear mems devices with taylor-series expansion and arnoldi approach. *Journal of Microelectromechanical Systems*, 13(3):441–451, 2004.

[63] A. A. Barlian, S.-J. Park, V. Mukundan, and B. L. Pruitt. Design and characterization of microfabricated piezoresistive floating element-based shear stress sensors. *Sensors and Actuators A: Physical*, 134(1):77–87, 2007.

[64] C.-S. Li, M.-H. Li, C.-H. Chin, and S.-S. Li. Differentially piezoresistive sensing for CMOS-MEMS resonators. *Journal of Microelectromechanical Systems*, 22(6):1361–1372, 2013.

[65] M. Koskenvuori and I. Tittonen. GHz-range FSK-reception with microelectromechanical resonators. *Sensors and Actuators A: Physical*, 142(1):346–351, 2008.

[66] J. J. Wortman and R. A. Evans. Young's modulus, shear modulus, and Poisson's ratio in silicon and germanium. *Journal of Applied Physics*, 36(1):153–156, 1965.

[67] L. F. Shampine and M. W. Reichelt. The MATLAB ODE suite. *SIAM Journal on Scientific Computing*, 18(1):1–22, 1997.

[68] G. Arndt, E. Colinet, J. Arcamone, and J. Juillard. A design methodology for fully integrated MEMS and NEMS pierce oscillators. *Sensors and Actuators A: Physical*, 172(1):293–300, 2011.

[69] S. S. Bedair and G. K. Fedder. CMOS MEMS oscillator for gas chemical detection. In *Proceedings of The 3rd IEEE Conference on Sensors*, pages 955–958, Vienna, Austria, 2004.

[70] G. Jourdan, E. Colinet, J. Arcamone, A. Niel, C. Marcoux, and L. Duraffourg. NEMS-based heterodyne self-oscillator. *Sensors and Actuators A: Physical*, 189(0):512–518, 2013.